

Kondo physics and dissipation: A numerical renormalization-group approach to Bose-Fermi Kondo models

Matthew T. Glossop* and Kevin Ingersent

Department of Physics, University of Florida, Gainesville, Florida 32611-8440, USA

(Dated: May 1, 2019)

We extend the numerical renormalization-group method to treat Bose-Fermi Kondo models (BFKMs) describing a local moment coupled both to a conduction band and to a dissipative bosonic bath representing, e.g., lattice or spin collective excitations of the environment. We apply the method to the Ising-symmetry BFKM with a structureless band and a bath spectral function $\eta(\omega) \propto \omega^s$. The method is valid for all bath exponents s and all temperatures T . For $0 < s < 1$, the range of interest in the context of heavy-fermion quantum criticality, an interacting critical point, characterized by hyperscaling of exponents and ω/T -scaling, describes a continuous quantum phase transition between Kondo-screened and localized phases. For Ohmic dissipation $s = 1$, where the model is relevant to certain dissipative mesoscopic qubit devices, the transition is found to be Kosterlitz-Thouless-like. In both regimes the impurity spectral function for the corresponding Anderson model shows clearly the collapse of the Kondo resonance at the transition. Connection is made to other recent results for the BFKM and the spin-boson model.

PACS numbers: 75.20.Hr, 71.10.Hf, 71.27.+a, 05.10.Cc

I. INTRODUCTION

Quantum impurity models that incorporate dissipative effects of the environment^{1,2} are highly topical. Applications of such models, which represent the environment by one or more bosonic baths, are numerous and include noisy quantum dots,^{3,4,5} decoherence of qubits in quantum computation,^{6,7,8,9} and charge transfer in biological donor-acceptor systems.^{10,11} Furthermore, within dynamical mean-field theory (DMFT) and its extensions, certain lattice models, of interest, e.g., in relation to heavy-fermion quantum criticality or the interplay of electrons and phonons in strongly correlated electron systems, also reduce to impurity problems of this nature.^{12,13} In this paper we provide a comprehensive account of the Ising-symmetry Bose-Fermi Kondo model (described further below) obtained via an extension of Wilson’s numerical renormalization-group method.¹⁴

The simplest example of a quantum impurity coupling to a bosonic bath is the celebrated spin-boson model (SBM), describing the dynamics of a two-state system coupled to a bath of harmonic oscillators. For a review see Ref. 1. The essential physics is the competition between the amplitude for tunnelling between the two spin states $S_z = \pm \frac{1}{2}$ (leading to a “delocalized phase”) and the effects of the environment embodied in the coupling, via S_z , to the bosonic bath, which tends to “localize” the system in one or other of the spin states. Not surprisingly, as the generic model for quantum dissipation, the SBM itself finds many applications in physics and chemistry.²

More general than the SBM are so-called “Bose-Fermi” quantum impurity problems involving both fermionic and bosonic baths. The Bose-Fermi Kondo model (BFKM) was originally discussed in the context of an extended dynamical mean-field theory (EDMFT) treatment of a two-band extended Hubbard model¹⁵ and describes a lo-

cal moment coupled not only to a fermionic conduction electron band — the “regular” Kondo model (for a review, see Ref. 16) — but also to a dissipative bosonic bath specified by a spectral function $B(\omega)$ that is typically modeled as $B(\omega) \propto \omega^s$ at low frequencies.

Of particular interest is the BFKM with a sub-Ohmic bath $s < 1$, which has been studied within a perturbative (in $\epsilon \equiv 1 - s$) renormalization group approach.^{15,17,18} The coupling of the impurity to the bosonic bath competes with the Kondo effect and leads, for $0 < s < 1$, to an unstable interacting critical point that describes a continuous quantum phase transition (QPT) between a Kondo-screened phase, in which the impurity moment is quenched by conduction electrons ($\langle S_z \rangle = 0$), and a localized phase where $\langle S_z \rangle \neq 0$. Thus, the BFKM provides an example of an *impurity* QPT, encapsulating the competition between local and spatially extended physics. For a recent review of impurity QPTs, see Ref. 19.

One possible direct realization of the Bose-Fermi Kondo model (BFKM) is a noisy metallic quantum dot: a large micron-scale dot coupled to a reservoir lead and subject to Ohmic dissipation ($s = 1$) arising via fluctuations in the gate voltage. Here, the two impurity “spin” states represent the two possible charge states of the dot close to a degeneracy point. Quantum charge fluctuations on the dot can be suppressed by voltage fluctuations, restoring perfect Coulomb-blockade staircase behavior.³ The model has also been invoked to study, within a dynamical large- N treatment, the quantum-critical Kondo effect in a single-electron transistor coupled to both the conduction electrons and spin waves of ferromagnetic leads.²⁰

However, to date the BFKM has received most attention in the context of heavy-fermion quantum criticality, arising in an EDMFT treatment of the Kondo lattice model.^{21,22,23,24} The Kondo lattice model is believed to capture the essential physics underlying heavy-

fermion QPTs: the dynamical competition between Kondo screening of f -shell moments on each lattice site by conduction electrons, which leads to a paramagnetic heavy-electron metallic phase; and antiferromagnetic ordering of those moments due to the Ruderman-Kittel-Kasuya-Yosida (RKKY) interaction. In EDMFT, which allows for the nonlocal quantum fluctuations arising from RKKY interactions between local moments, all correlation functions of the Kondo lattice problem can be calculated from a self-consistent Bose-Fermi Kondo model. Here, the bosonic bath embodies the effects, at a given site, of the fluctuating magnetic field generated (via the RKKY interaction) by local moments at other lattice sites.

The above is of considerable current interest in connection with so-called *local* quantum criticality. In this scenario of a heavy-fermion QPT, destruction of the Kondo effect accompanies divergence of the spatial correlation length at the antiferromagnetic ordering transition. Such a local quantum-critical point may arise within EDMFT — as a critical impurity solution satisfying the self-consistency — when magnetic spin fluctuations are two-dimensional.^{21,22} The salient non-Fermi liquid features of several materials, including $\text{CeCu}_{5.9}\text{Au}_{0.1}$, which resist the standard spin-density wave description,²⁵ appear to be consistent with a critical point of this nature. However, whether or not a local quantum-critical point (QCP) arises self-consistently under a nonperturbative treatment that considers both paramagnetic and antiferromagnetic phases of the model, is an important question and one that has not been satisfactorily answered by recent quantum Monte Carlo studies.^{26,27,28} These studies reach opposing conclusions concerning the nature of the $T = 0$ transition, in part due to the inherent limitations of accessing the lowest temperature scales within quantum Monte Carlo. Similar EDMFT mappings to a BFKM have been applied to the disordered Kondo lattice model to study interplay of Kondo screening and RKKY interactions in electronic Griffiths phases,²⁹ and to a t - J model of a highly incoherent metal close to a Mott transition,³⁰ of possible relevance to the pseudogap phase of the cuprates.

Bose-Fermi impurity problems may also arise through a conventional DMFT treatment of lattice models that include both electron correlation and electron-phonon interactions. The Hubbard-Holstein model is the simplest such model^{31,32,33} and has been discussed in connection with cuprate high- T_c superconductors, heavy-fermion systems, manganites and fulleride superconductivity. For a recent discussion of Bose-Fermi impurity problems in the context of DMFT, see Ref. 12.

The preceding remarks serve to motivate the study of Bose-Fermi impurity problems as a route to the description of a variety of physically relevant models of strongly-correlated systems. To what extent the impurity models (or impurity models plus DMFT self-consistency for lattice models) capture the relevant physical behavior can only be assessed if a reliable impurity solver is employed.

Such a technique should be capable of handling static and dynamical properties for all interaction strengths, bosonic bath spectra and temperatures. This is a demanding requirement, even for purely fermionic impurity models, and many of the standard techniques developed for the latter are here simply inapplicable. It is natural to turn to Wilson's nonperturbative numerical renormalization-group (NRG) method,¹⁴ which has so far provided a controlled numerical treatment of the thermodynamics, dynamical response functions, and transport properties of a range of fermionic impurity models and of lattice models within DMFT. Recent impurity-model applications include studies of quantum criticality in the pseudogap Kondo³⁴ and Anderson³⁵ models, unconventional physics in double quantum dots,^{36,37,38,39} and non-Fermi liquid behavior in a frustrated three-impurity Kondo model.⁴⁰ Applications to lattice systems include studies of the Mott-Hubbard metal-insulator transition in the Hubbard model⁴¹ and the paramagnetic phase of the periodic Anderson model relevant to heavy-fermion systems.⁴² For a review, see, e.g., Ref. 43. The scope of potential applications of the NRG method has recently been widened following a successful treatment of the spin-boson model via a pure bosonic NRG.^{44,45} The latter has provided a good account of the critical properties of the SBM for both Ohmic and sub-Ohmic bath spectra.

This paper reports a direct study of the Bose-Fermi Kondo model using an NRG method extended to handle *simultaneously* both fermionic and bosonic degrees of freedom. We demonstrate that our approach provides a good account of the critical properties of the Ising-symmetry BFKM for both a sub-Ohmic bosonic bath with $s < 1$, as reported briefly in Ref. 46, and for the transition in the Ohmic case $s = 1$. We provide an important confirmation that the Ising-BFKM and SBM belong to the same universality class, as implied by bosonization. The NRG treatment described is reliable for all bosonic bath exponents and temperatures. Importantly, it opens the way for a reliable numerical solution of the Kondo lattice model by imposing EDMFT self-consistency on the BFKM solution, as we have discussed elsewhere.²³

The paper is organized as follows. After the essential background to the BFKM is given in Sec. II, an outline of the NRG treatment of the model — which involves logarithmic discretization of the energy axis, mapping of the Hamiltonian to a chain form, and the iterative numerical solution of the problem at a sequence of decreasing energy scales — is given in Sec. III.

Results arising from the approach are presented in two parts, beginning with the case of sub-Ohmic dissipation in Sec. IV. The flow of the NRG transformation and its fixed points is discussed in Sec. IV A. An interacting critical fixed point separates a Kondo-screened phase, for weak coupling to the bosonic bath, from a strong-coupling localized phase with no Kondo resonance. The form of the phase boundaries, in particular the relationship of the critical coupling to the bosonic bath exponent and the Kondo scale of the pure-fermionic problem,

is discussed in Sec. IV B. In Sec. IV C, for $0 < s < 1$, we determine the correlation-length exponent that governs the vanishing, at the quantum-critical point, of a low-energy crossover scale. The response to a local magnetic field applied at the impurity site provides a useful probe of impurity quantum phase transitions; in Sec. IV D we discuss the static and dynamical local susceptibility. Distinct behavior obtains in either stable phase and at the QCP. Critical behavior is manifest as power laws (with anomalous exponents) in the temperature and frequency dependences, which reflect the fact that the critical physics is scale-free. We identify an order parameter for the problem, which, for $0 < s < 1$, vanishes continuously as the transition is approached. Various critical exponents are extracted and are shown to obey hyperscaling relations. The latter, together with ω/T -scaling at the critical point, are consistent with an interacting fixed point. In Sec. IV E we consider the single-particle spectral function $A(\omega)$, in which the collapse of the Kondo resonance at the QCP is directly manifest. The critical properties and scaling behavior are discussed in detail.

The nature of the transition changes qualitatively at $s = 1$, as reflected in the divergence of the correlation length exponent as $s \rightarrow 1^-$. We consider the Ohmic case ($s = 1$) in Sec. V, demonstrating that the transition is Kosterlitz-Thouless-like, with characteristic vanishing of the renormalized Kondo scale and a jump in the order parameter at the critical coupling. The spectral function and its scaling properties are discussed and compared to their sub-Ohmic counterparts. We also briefly examine our results in the context of the noisy quantum box.^{3,4,5}

The paper concludes with a brief summary and outlook for future work.

II. BACKGROUND

In the remainder of this paper we focus on the Bose-Fermi Kondo model with Ising anisotropy in the bosonic couplings. This is the case most relevant to the EDMFT treatment of $\text{CeCu}_{6-x}\text{Au}_x$ and to the noisy quantum dot system. We treat the model by extending the NRG method to encompass Bose-Fermi impurity problems. Though described in Sec. III for the Ising-BFKM, the approach is straightforwardly generalized to the xy and isotropic problems. Results for the latter cases will be discussed elsewhere. In the following subsection we define the model to be studied and identify key quantities, before going on to discuss the connection to the spin-boson model in Sec. II B. We set $\hbar = g\mu_B = k_B = 1$.

A. Ising-anisotropic Bose-Fermi Kondo model

The Hamiltonian for the Ising-symmetry Bose-Fermi Kondo model is given by

$$\hat{H} = \hat{H}_F + \hat{H}_B + \hat{H}_{\text{int}}, \quad (2.1)$$

where

$$\hat{H}_F = \sum_{\mathbf{k}, \sigma} \epsilon_{\mathbf{k}} c_{\mathbf{k}\sigma}^\dagger c_{\mathbf{k}\sigma} \quad (2.2)$$

and

$$\hat{H}_B = \sum_{\mathbf{q}} \omega_{\mathbf{q}} \phi_{\mathbf{q}}^\dagger \phi_{\mathbf{q}} \quad (2.3)$$

describe, respectively, the conduction band and a dissipative bosonic bath. Both are taken to be noninteracting and characterized by the densities of states

$$\rho(\epsilon) = \sum_{\mathbf{k}} \delta(\epsilon - \epsilon_{\mathbf{k}}) \quad (2.4)$$

and

$$\eta(\omega) = \sum_{\mathbf{q}} \delta(\omega - \omega_{\mathbf{q}}). \quad (2.5)$$

The interaction of the impurity with the baths is contained in

$$\hat{H}_{\text{int}} = \frac{1}{2} J_0 \mathbf{S} \cdot \sum_{\mathbf{k}, \mathbf{k}', \sigma, \sigma'} c_{\mathbf{k}\sigma}^\dagger \boldsymbol{\sigma}_{\sigma\sigma'} c_{\mathbf{k}'\sigma'} + S_z \sum_{\mathbf{q}} g_{\mathbf{q}} (\phi_{\mathbf{q}} + \phi_{-\mathbf{q}}^\dagger). \quad (2.6)$$

The first term describes the interaction of a spin- $\frac{1}{2}$ local moment with the on-site spin of the fermionic band via the usual Kondo coupling J_0 ; the second term describes its coupling, of magnitude $g_{\mathbf{q}}$, to the bosonic bath with oscillators $\{\phi_{\mathbf{q}}\}$.

We assume a featureless metallic host conduction band of width $2D$ described by a density of states

$$\rho(\epsilon) = \rho_0 \Theta(D - |\epsilon|) \quad (2.7)$$

with $\Theta(x)$ the Heaviside step function. The bosonic bath is entirely determined by the spectral function

$$B(\omega) = \pi \sum_{\mathbf{q}} g_{\mathbf{q}}^2 \delta(\omega - \omega_{\mathbf{q}}), \quad (2.8)$$

which we assume vanishes outside the range $0 < \omega < \omega_0$. Note that the bath density of states $\eta(\omega)$ and coupling $g_{\mathbf{q}}$ do not require separate specification. Writing $x = \epsilon/D$ and $y = \omega/\omega_0$, the Hamiltonian is conveniently written in the following one-dimensional form:

$$\hat{H}_F + \hat{H}_B = D \int_{-1}^{+1} dx x c_{x\sigma}^\dagger c_{x\sigma} + \omega_0 \int_0^1 dy y \phi_y^\dagger \phi_y, \quad (2.9a)$$

$$\hat{H}_{\text{int}} = D \rho_0 J_0 \mathbf{S} \cdot \sum_{\sigma\sigma'} f_{0\sigma}^\dagger \boldsymbol{\sigma}_{\sigma\sigma'} f_{0\sigma'} + \omega_0 \sqrt{\frac{B_0 \mathcal{B}^2}{\pi}} S_z (b_0 + b_0^\dagger), \quad (2.9b)$$

extracting a dimensionless ‘‘dissipation strength’’ B_0 from $B(\omega)$. The dimensionless operators

$$f_{0\sigma} = \frac{1}{\sqrt{2}} \int_{-1}^{+1} dx c_{x\sigma} \quad (2.10)$$

and

$$b_0 = \mathcal{B}^{-1} \int_0^1 dy W(y) \phi_y, \quad (2.11)$$

the latter defined by a weighting function

$$W(y) = \sqrt{\frac{B(\omega_0 y)}{B_0 \omega_0}} \quad (2.12)$$

and a normalization factor

$$\mathcal{B}^2 = \int_0^1 dy W^2(y), \quad (2.13)$$

respectively annihilate the unique combination of fermions and bosons that couples to the impurity. The operators $c_{x\sigma}$ and ϕ_y obey the commutation relations $\{c_{x\sigma}^\dagger, c_{x'\sigma'}\} = \delta(x - x')\delta_{\sigma\sigma'}$ and $[\phi_y^\dagger, \phi_{y'}] = \delta(y - y')$ respectively, while $\{f_{0\sigma}^\dagger, f_{0\sigma'}\} = \delta_{\sigma\sigma'}$ and $[b_0, b_0^\dagger] = 1$.

Of principal interest is the low-temperature physics of the model, determined by the form of the bath spectrum at low energies. We take $B(\omega)$ to be given by

$$B(\omega) = \begin{cases} B_0 \omega_0^{1-s} \omega^s & \text{for } 0 < \omega < \omega_0, \\ 0 & \text{otherwise,} \end{cases} \quad (2.14)$$

with $s > -1$ necessarily. The bulk of the paper concerns the sub-Ohmic regime $s < 1$; in particular we focus on $0 < s < 1$ where the key physics is governed by an interacting quantum-critical point. However, we also study the Ohmic case ($s = 1$) in Sec. V.

To connect with previous work on the BFKM, we will assume that $g_{\mathbf{q}}$ is \mathbf{q} -independent ($g_{\mathbf{q}} \equiv g_0$) and that the bath spectral function is of form

$$\eta(\omega) = \begin{cases} (K_0^2/\pi) \omega_0^{1-s} \omega^s & \text{for } 0 < \omega < \omega_0 \\ 0 & \text{otherwise,} \end{cases} \quad (2.15)$$

and hence, from Eqs. (2.8) and (2.5), $B_0 \equiv (K_0 g_0)^2$.

B. Connection to the spin-boson model

The spin-boson model is the simplest model of quantum dissipation,¹ describing a two-level system coupled to a bosonic bath:

$$\hat{H}_{SB} = \hat{H}_B - \Delta S_x + \epsilon S_z + S_z \sum_{\mathbf{q}} \lambda_{\mathbf{q}} (\phi_{\mathbf{q}} + \phi_{-\mathbf{q}}^\dagger). \quad (2.16)$$

Here, Δ is the amplitude for tunneling between the “spin” states $S_z = \pm \frac{1}{2}$, and ϵ represents an additional bias. The coupling to the environment is characterized by the spectral function $J(\omega) = \pi \sum_{\mathbf{q}} \lambda_{\mathbf{q}}^2 \delta(\omega - \omega_{\mathbf{q}})$. It is well known¹ that there exists a correspondence between the Ohmic spin-boson model and the anisotropic Kondo model (AKM), described by a Hamiltonian $\hat{H} =$

$\hat{H}_F + \hat{H}_{\text{int}}$ with \hat{H}_F given by Eqs. (2.2), (2.4) and (2.7), and

$$\begin{aligned} \hat{H}_{\text{int}} &= \frac{J_{\perp}}{2} \sum_{\mathbf{k}, \mathbf{k}'} (c_{\mathbf{k}\uparrow}^\dagger c_{\mathbf{k}'\downarrow} S^- + c_{\mathbf{k}\downarrow}^\dagger c_{\mathbf{k}'\uparrow} S^+) \\ &+ \frac{J_z}{2} \sum_{\mathbf{k}, \mathbf{k}'} (c_{\mathbf{k}\uparrow}^\dagger c_{\mathbf{k}'\uparrow} - c_{\mathbf{k}\downarrow}^\dagger c_{\mathbf{k}'\downarrow}) S^z + h S^z. \end{aligned} \quad (2.17)$$

Specifically, following bosonization of the AKM (see, e.g., Ref. 47),

$$\epsilon = g \mu_B h, \quad (2.18)$$

$$\frac{\Delta}{\omega_c} = \rho_0 J_{\perp}, \quad (2.19)$$

$$J(\omega) = 2\pi\alpha\omega \quad \text{for } \omega < \omega_c, \quad (2.20)$$

where the dimensionless dissipation strength $\alpha = [1 - (2/\pi) \tan^{-1}(\pi\rho_0 J_z/4)]^2$ and $\omega_c = 2D$.

The Ohmic case of the SBM is well understood. The essential physics is a Kosterlitz-Thouless quantum phase transition between a delocalized phase for $\alpha < \alpha_c$ — in which the effect of dissipation is to renormalize the tunneling amplitude — and a localized phase for $\alpha > \alpha_c$, where tunneling between the spin states is absent. For $\Delta \rightarrow 0$, $\alpha_c = 1$. Thus, the Kondo scale T_K of the AKM can be interpreted as a renormalization of the bare tunneling amplitude $\rho_0 J_{\perp}$ due to frictional effects of the electronic environment (particle-hole excitations) controlled by $\rho_0 J_z$. The antiferromagnetic phase of the AKM corresponds to the delocalized phase of the SBM, while the ferromagnetic sector corresponds to the localized phase. For the regular isotropic Kondo model, $J_z = J_{\perp} \equiv J_0$, the corresponding SBM dissipation strength takes the value $\alpha = 1^-$ for $\rho_0 J_0 \ll 1$.

The SBM with sub-Ohmic dissipation has only recently been studied in detail, using perturbative⁴⁸ and numerical renormalization group⁴⁴ methods. For bath exponents $0 < s < 1$ these studies establish the existence of an interacting quantum-critical point describing a continuous QPT between delocalized and localized phases, with $\alpha_c \propto \Delta^{1-s}$ for $\Delta \ll \omega_c$.

Recent studies of the Ising-symmetry Bose-Fermi Kondo model with Ohmic dissipation^{4,5} have exploited the connection between the AKM and Ohmic SBM. For example, the essential results of Ref. 45 have been discussed in the context of the Ohmic BFKM,⁴ of relevance to certain dissipative mesoscopic qubit devices. More generally, the Ising-symmetry BFKM can be mapped to a spin-boson model whose spectral function $J(\omega)$ comprises an Ohmic contribution from the bosonized conduction band and a contribution $B(\omega) \propto \omega^s$ from the BFKM bath. The resulting $J(\omega)$ is dominated by $B(\omega)$ at low frequencies and thus it is to be expected that the Ising symmetry BFKM and SBM have identical universal critical properties for $s \leq 1$. However, the presence of the Ohmic contribution acts to renormalize the bare tunneling amplitude entering the model, such that the sub-Ohmic BFKM corresponds to a SBM, Eq. (2.16),

with $J(\omega) \propto \omega^s$ for $\omega \ll \omega_c$ and the bare Kondo scale T_K (not J) the appropriate tunneling amplitude. This is borne out by the numerical results of Sec. IV.

III. NRG TREATMENT

In Wilson's original NRG treatment of the Kondo model¹⁴ [as described by $\hat{H} = \hat{H}_F + \hat{H}_{\text{int}}$, Eqs. (2.2), (2.6) with $g_{\mathbf{q}} = 0$, and (2.7)] the conduction band continuum of energies ϵ is sampled at the discrete set of energies $\epsilon = \pm D\Lambda^{-m}$ for $m = 0, 1, 2, \dots$, where $\Lambda > 1$ parametrizes the discretization. By a mapping of \hat{H}_F to a tight-binding Hamiltonian using the Lanczos procedure, the Kondo Hamiltonian is cast in the form of a semi-infinite fermionic chain with the impurity coupled only to the end site $n = 0$. Owing to the discretization, the tight-binding coefficients decay with site number as $D\Lambda^{-n}$ for large n , which feature allows for an iterative solution to the problem by numerically diagonalizing the Hamiltonian for progressively longer finite chains. The procedure amounts to including excitations on an exponentially smaller energy scale at each step, with the full Hamiltonian being recovered as the limit

$$\hat{H} = \lim_{N \rightarrow \infty} \alpha \Lambda^{-N/2} D H_N. \quad (3.1)$$

Here, \hat{H}_N describes an $(N + 1)$ -site (fermionic) chain, rescaled so that the lowest energy is of order unity and a meaningful comparison between the $\{\hat{H}_N\}$ can be made. The constant α is conventional and given by $\alpha = \frac{1}{2}\Lambda^{\frac{1}{2}}(1 + \Lambda^{-1})$.

The renormalization-group transformation \hat{R} , defined by $H_N = \hat{R}H_{N-1}$, eventually reaches a scale-invariant fixed point of \hat{R}^2 that determines the low-temperature properties of the system. At a fixed point, the low-lying eigenstates and matrix elements of any observable operator are identical for iterations N and $N - 2$. That the fixed points are of the transformation \hat{R}^2 and not \hat{R} reflects the fundamental inequivalence of fermionic chains containing odd and even numbers of sites, as discussed, e.g., in Ref. 49.

In the following we outline the transformation of the BFKM, Eqs. (2.1) and (2.9), to the form required for an NRG treatment. Including a coupling between the impurity and a bosonic bath introduces two additional considerations. First, and most obviously, the bosonic Hilbert space must be truncated from the outset, introducing a bosonic truncation parameter. The effects of this truncation on the critical properties of interest must be systematically studied. Second, the iterative procedure employed must preserve the spirit of the NRG approach, taking into account all excitations of the same energy scale at the same iteration. We turn to a discussion of these issues in the following section.

A. Discretization and mapping

The bosonic bath [conduction band] continuum of energies $0 \leq \omega \leq \omega_0$ [$-D \leq \epsilon \leq D$] is replaced by a discrete set: $\omega_0 \Lambda^{-m}$ [$\pm D \Lambda^{-m}$] for integer $m \geq 0$. The main approximation of the NRG is to select just one bosonic [fermionic] state from each energy interval. We retain the single state that couples directly to the impurity such that b_0 in Eq. (2.11) is given exactly by

$$b_0 = \mathcal{B}^{-1} \sum_m \mathcal{B}_m \phi_m \quad (3.2)$$

with

$$\phi_m = \mathcal{B}_m^{-1} \int_{\Lambda^{-(m+1)}}^{\Lambda^{-m}} dy W(y) \phi_y \quad (3.3)$$

and

$$\mathcal{B}_m^2 = \int_{\Lambda^{-(m+1)}}^{\Lambda^{-m}} dy W^2(y). \quad (3.4)$$

For the fermions,

$$f_{0\sigma} = \frac{1}{\sqrt{2}} \sum_m (c_{m\sigma}^> + c_{m\sigma}^<). \quad (3.5)$$

The operators $c_{m\sigma}^>$ and $c_{m\sigma}^<$ are defined for the m th positive and negative energy intervals respectively and are given by

$$c_{m\sigma}^> = \int_{\Lambda^{-(m+1)}}^{\Lambda^{-m}} dx c_{x\sigma}, \quad (3.6)$$

$$c_{m\sigma}^< = \int_{-\Lambda^{-m}}^{-\Lambda^{-(m+1)}} dx c_{x\sigma}. \quad (3.7)$$

The terms \hat{H}_B and \hat{H}_F are then approximately written as

$$\hat{H}_B \simeq \omega_0 \sum_m^\infty \omega_m \phi_m^\dagger \phi_m, \quad (3.8)$$

$$\hat{H}_F \simeq D \sum_m^\infty (\epsilon_m^> c_{m\sigma}^> c_{m\sigma}^>\dagger + \epsilon_m^< c_{m\sigma}^<\dagger c_{m\sigma}^<), \quad (3.9)$$

where

$$\omega_m = \mathcal{B}_m^{-2} \int_{\Lambda^{-(m+1)}}^{\Lambda^{-m}} dy W(y)y, \quad (3.10)$$

$$\epsilon_m^\gtrless = \pm \frac{1}{2} (\Lambda^{-m} + \Lambda^{-(m+1)}), \quad (3.11)$$

and the approximation is seen to amount to selecting the state of weighted mean energy from each interval.

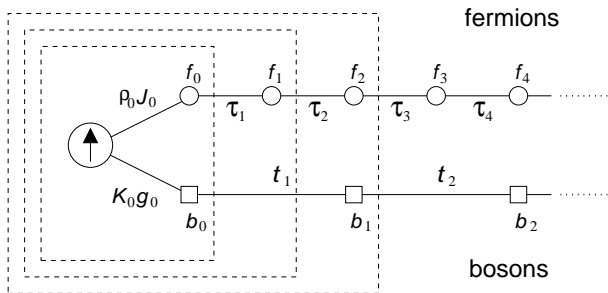


FIG. 1: Schematic of the chain form of the BFKM Hamiltonian. Fermionic sites of the tight-binding chain are shown as small circles, while bosonic sites are shown as squares. Only the end site of each chain couples directly to the impurity spin. The coupling between the fermionic sites decays as $\tau_n \sim \Lambda^{-n/2}$ for large n , while the bosonic couplings fall off as $t_n \sim \Lambda^{-n}$. The dashed boxes enclose, from innermost to outermost, the sites included in iterations 0, 1, and 2, respectively.

The infinite number of states neglected in each interval are orthogonal to the state retained and couple only indirectly to the impurity, which coupling vanishes as $\Lambda \rightarrow 1$. As is standard in the NRG approach, we neglect this coupling for $\Lambda > 1$ and drop the irrelevant decoupled constant term that thereby results. The discretization error incurred vanishes as $\Lambda \rightarrow 1$, which fact alone favors choosing Λ close to unity. One manifestation of discretization error is a modification of the effective coupling between impurity and bosonic bath [conduction band]. Essentially exact results, if desired, can be obtained by performing a $\Lambda \rightarrow 1^+$ extrapolation from $\Lambda > 1$ results. Fortunately, critical exponents are often found to be extremely insensitive to the chosen Λ . Larger Λ (e.g., $\Lambda = 9$) calculations, which retain fewer states and thus require less computational effort, can then be used to extract the critical properties of the model. However, the weak Λ -dependence of critical exponents cannot of course be assumed at the outset.

Finally, Eqs. (3.8) and (3.9) are mapped exactly onto tight-binding Hamiltonians via a discretized Lanczos procedure.⁵⁰ Defining

$$b_n = \sum_m u_{nm} \phi_m, \quad (3.12)$$

$$f_{n\sigma} = \sum_m (v_{nm}^> c_{m\sigma}^> + v_{nm}^< c_{m\sigma}^<), \quad (3.13)$$

where $u_{0m} = \mathcal{B}_m/\mathcal{B}$ and $v_{0m}^{\geq} = 1/\sqrt{2}$, such that $[b_n, b_{n'}^\dagger] = \delta_{n,n'}$ and $\{f_{n\sigma}, f_{n'\sigma'}^\dagger\} = \delta_{n,n'} \delta_{\sigma,\sigma'}$, we obtain

$$\hat{H}_B = \omega_0 \sum_n \left[e_n b_n^\dagger b_n + t_n (b_n^\dagger b_{n-1} + b_{n-1}^\dagger b_n) \right], \quad (3.14)$$

$$\hat{H}_F = D \sum_{n,\sigma} \left[\epsilon_n f_{n\sigma}^\dagger f_{n\sigma} + \tau_n (f_{n\sigma}^\dagger f_{n-1,\sigma} + f_{n-1,\sigma}^\dagger f_{n\sigma}) \right]. \quad (3.15)$$

The tight-binding coefficients ϵ_n , τ_n , e_n and t_n ($n = 0, 1, 2, \dots$) encode all information about the conduction band and bosonic bath and are determined numerically, for given $B(\omega)$ and $\rho(\omega)$, via Lanczos recursion relations. For example, e_n and t_n follow from numerically iterating

$$\begin{aligned} \sum_m u_{nm}^2 \omega_m &= e_n, \\ u_{nm}(\omega_m - e_n) - t_n u_{n-1,m} &= t_{n+1} u_{n+1,m}, \\ \sum_m u_{n+1,m}^2 &= 1, \end{aligned} \quad (3.16)$$

with ω_m given by Eq. (3.10). For a symmetric fermionic band density of states $\rho(\epsilon) = \rho(-\epsilon)$, $\epsilon_n = 0$ for all n . For the specific case Eq. (2.7) considered in the following, we use the closed-form algebraic expression for τ_n as derived by Wilson.¹⁴ The transformed Hamiltonian to be solved, $\hat{H} = \hat{H}_F + \hat{H}_B + \hat{H}_{\text{int}}$ [Eqs. (2.9), (3.14) and (3.15)], describes two semi-infinite chains each coupled at the end site only to a spin- $\frac{1}{2}$ magnetic moment. A schematic of the chain form of the Hamiltonian is depicted in Fig. (1).

B. Iterative solution

The on-site energies ϵ_n and hopping coefficients τ_n for the fermionic tight-binding chain decrease like $\Lambda^{-n/2}$ for large chain length n . The hopping coefficients for the bosonic chain, e_n and t_n , drop off faster — as Λ^{-n} for large n — arising because the spectral density $B(\omega)$ is nonzero for $\omega > 0$ only. The latter fact has been discussed in the context of a pure *bosonic* NRG approach to the spin-boson model,^{44,45} and there allows a convergent approximation using a single bosonic chain of finite length. While the BFKM mapping is essentially a combination of the pure fermionic and pure bosonic approaches, the iterative procedure described below is an important novel feature of our approach, and one that does not *a priori* guarantee a satisfactory description of the quantum-critical physics of the model.

In employing the NRG for the BFKM we must ensure that at each step we treat only fermions and bosons of the same energy scale. As for the pure fermionic case, we take D as the energy unit and write the full Hamiltonian as the limit Eq. (3.1), where here N refers to the highest labelled fermionic site or iteration number. Crucially, the following recursion relation, relating H_N to $H_{N-1}(M-1)$, adds site M to the bosonic chain only if its tight-binding coefficients are comparable to the energy scale ($\Lambda^{-N/2}$) set by the fermionic site N added at the current

iteration, N . Thus,

$$\begin{aligned}
H_N &= \Lambda^{\frac{1}{2}} H_{N-1} (M-1) + \alpha^{-1} \Lambda^{N/2} \sum_{\sigma} \epsilon_N f_{N\sigma}^{\dagger} f_{N\sigma} \\
&+ \alpha^{-1} \Lambda^{N/2} \sum_{\sigma} \tau_N (f_{N\sigma}^{\dagger} f_{N-1,\sigma} + \text{H.c.}) \\
&+ \tilde{\omega}_0 \alpha^{-1} \Lambda^{N/2} \Theta(\xi_M - c \Lambda^{-N/2}) \left[e_M b_M^{\dagger} b_M \right. \\
&\left. + t_M (b_M^{\dagger} b_{M-1} + \text{H.c.}) \right] \quad (3.17)
\end{aligned}$$

where $\tilde{\omega}_0 = \omega_0/D$, $\xi_M = \max(e_M, t_M)$ and c is a threshold parameter that we typically assign the value $c = \Lambda^{-1/4}$. The Hamiltonian for iteration $N = 0$, containing the couplings between the impurity and the end site of each chain, is given by

$$\begin{aligned}
\alpha H_0 &= \sum_{\sigma\sigma'} \rho_0 J_0 \mathbf{S} \cdot f_{0\sigma}^{\dagger} \sigma_{\sigma\sigma'} f_{0\sigma'} + \sum_{\sigma} \epsilon_0 f_{0\sigma}^{\dagger} f_{0\sigma} \\
&+ \tilde{\omega}_0 \sqrt{\frac{B_0 \mathcal{B}^2}{\pi}} S_z (b_0^{\dagger} + b_0) + \tilde{\omega}_0 \epsilon_0 b_0^{\dagger} b_0, \quad (3.18)
\end{aligned}$$

with natural dimensionless parameters $\rho_0 J_0$, $B_0 \equiv (K_0 g_0)^2$ and $\tilde{\omega}_0 = \omega_0/D$ to be varied for a given exponent s in the bath spectral function $B(\omega)$ [Eq. (2.8)].

Since both e_n and t_n decay as Λ^{-n} for large chain length n , the iterative procedure Eq. (3.17) rapidly amounts to extending the bosonic chain at every second iteration (i.e., for every second site added to the fermionic chain). Thus without any change in the essential physical properties, it is possible, and proves convenient, to modify Eq. (3.17) to force the extension of the bosonic chain to occur only at a given iteration parity.

We also note in passing that an alternative NRG scheme for the BFKM might extend both chains at each iteration but employ a different discretization parameter Λ_B for bosonic energies related to that for fermionic energies Λ_F by $\Lambda_F = \Lambda_B^2$ (Ref. 51). Though such a scheme has not yet been implemented, we believe it does not confer any significant advantages over the approach taken in this work.

The eigenstates $\{|E\rangle_{N-1}\}$ of H_{N-1} are used to construct the basis states for iteration N :

$$|l, E\rangle_N = |E\rangle_{N-1} \otimes |l\rangle_N. \quad (3.19)$$

where $\{|l\rangle_N\}$ are the states of the added site(s). If the fermionic chain alone is extended then $|l\rangle_N \equiv |i\rangle_N$, one of the four possible states of the added fermionic site. If both a fermionic and a bosonic site are added, then $|l\rangle_N = |i\rangle_N \otimes |n_M\rangle$ where $\{|n_M\rangle\}$ is an eigenstate of $b_M^{\dagger} b_M$. In contrast to fermionic sites, the number of bosons per site of the bosonic chain is in principle unlimited. In practice, the bosonic Hilbert space must be truncated, restricting the maximum number of bosons per site of the bosonic chain to a finite number N_b , typically $N_b \leq 16$ and thus including only the lowest $N_b + 1$ eigenstates of $b_M^{\dagger} b_M$. We have systematically studied the effects of this truncation on various properties of the

BFKM. In particular, we find that universal critical properties rapidly converge with increasing N_b — typically $8 < N_b < 16$ suffices — providing a very satisfactory description of the QCP for the model. This is discussed further in Sec. IV.

It follows from Eqs. (3.17) and (3.19) that the matrix elements of H_N , ${}_N \langle l', E' | H_N | l, E \rangle_N$, can be evaluated in terms of the eigenstates and eigenenergies of H_{N-1} and the matrix elements ${}_N \langle i' | f_N^{\dagger} | i \rangle_N$ and, if appropriate, ${}_M \langle n' | b_M^{\dagger} | n \rangle_M$. The numerical effort required to diagonalize H_N is considerably reduced by taking advantage of various symmetries of the Hamiltonian, as discussed, e.g., in Refs. 49 and 34. With H_N diagonalized, the matrix elements of H_{N+1} are formed in the basis Eq. (3.19) with $N \rightarrow N+1$ and the procedure is repeated to obtain the many-body spectrum on progressively lower energy scales.

The need for an iterative approach arises because (even after bosonic truncation) the size of the basis rapidly becomes unmanageable. For the regular Kondo model it grows by a factor of 4 at each iteration, reflecting the possible occupancies of the added fermionic site. Even in that relatively simple application, finite computational power demands that the basis be truncated after only a few iterations, saving only the lowest N_s many-body eigenstates of H_{N-1} to be used to construct the basis in which to diagonalize H_N . The problem is of course even more acute in the BFKM: for each iteration that a bosonic site is added to the chain the basis grows by a factor of $4(N_b + 1)$.

By retaining only the lowest N_s eigenstates from one iteration to the next, the NRG method gives a sequence of truncated Hamiltonians from which thermodynamic [dynamical] properties may be calculated. For each iteration N , the error due to truncation is minimized in a temperature [frequency] window around a characteristic energy scale

$$T_N = \alpha \Lambda^{-N/2} / \bar{\beta}, \quad (3.20)$$

where $\bar{\beta} < 1$ is a dimensionless parameter³⁴ that generally decreases with increasing N_s . Properties at temperature [frequency] scales smaller than T_N will be more accurately calculated at subsequent iterations, while those at higher scales have been more accurately calculated at a previous iteration. See, e.g., Refs. 49 and 52 for further discussion.

In the following we turn to results arising from the above approach, beginning with the case of sub-Ohmic dissipation.

IV. RESULTS: SUB-OHMIC DISSIPATION

We now consider results for the Bose-Fermi Kondo model with sub-Ohmic dissipation, i.e., $s < 1$ in Eq. (2.14). The Ohmic case $s = 1$ is discussed separately in Sec. V. For $0 < s < 1$ the model exhibits a continu-

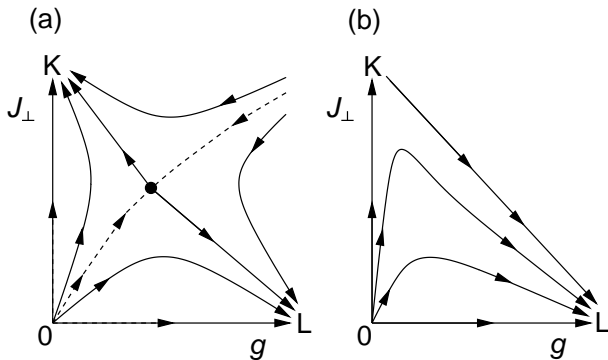


FIG. 2: Schematic of the NRG flow of effective couplings for (a) $0 < s < 1$ and (b) $-1 < s \leq 0$. Trajectories describe the flow with increasing N (or decreasing T_N) of the effective J_\perp and g that enter H_N . For $0 < s < 1$ an unstable critical fixed point (solid circle) lies on the separatrix (dashed line) that specifies the phase boundary between the stable Kondo (K) and localized (L) phases in the J_\perp - g plane. The Kondo fixed point corresponds to an effective $J_\perp = J_z = \infty$ and $g = 0$, while the localized fixed point has $J_\perp = 0$, J_z finite, and $g = \infty$. For $-1 < s \leq 0$ the localized fixed point is reached for all $g \neq 0$. See text for further discussion.

ous impurity quantum phase transition between Kondo-screened and unscreened-local-moment phases. After discussing the NRG flows, fixed points and phase boundaries, we demonstrate that a low-energy scale T_* , characterizing the crossover from critical to stable fixed point behavior, vanishes in a power-law fashion at the quantum-critical point. Local magnetic properties considered in Sec. IVD show distinct behaviors in either phase and at the QCP itself, from which various critical exponents can be extracted. The interacting nature of the QCP is evident from hyperscaling of the critical exponents, including ω/T -scaling behavior in the dynamics. We conclude the discussion of the sub-Ohmic case by considering the local spectrum of single-particle excitations for the related Bose-Fermi Anderson model. The destruction of the central Kondo resonance at the QCP is clearly observed.

For notational compactness we write henceforth $\rho_0 J_0 \equiv J$ and $K_0 g_0 \equiv g$. We also set the bosonic bath cut-off $\tilde{\omega}_0 = 1$ in our calculations,⁵³ although we emphasize that our approach is in no way limited to this particular choice. All energies, frequencies, and temperatures are expressed as multiples of $D = 1$. For a given bath exponent s , we typically work at fixed J and vary g to tune the system through a quantum phase transition. However, in calculations of the single-particle spectrum, we specify $B_0 \equiv g^2$. Critical properties are found to be insensitive to the NRG discretization parameter Λ and adequately converged for bosonic truncation parameter $8 < N_b < 12$. Unless stated otherwise, results presented were obtained using $\Lambda = 9$, $N_b = 8$ and $N_s = 500$.

A. NRG flow and fixed points

Figure 2(a) shows a schematic of the NRG flow of effective couplings found for $0 < s < 1$. There are two stable fixed points of the flow: the familiar Kondo fixed point (K), where the impurity spin is screened by conduction electrons and the single-particle spectrum contains a Kondo resonance (see Sec. IVE); and a “localized” fixed point (L), where the impurity dynamics are controlled by coupling to the dissipative bath. A third fixed point — the unstable, critical fixed point (where Kondo screening is critical) — lies on the separatrix $g = g_c(J)$ which specifies the phase boundary in the J - g plane (see Sec. IVB).

As an example, Fig. 3 shows the NRG flow of the low-lying eigenenergies of H_N as a function of even iteration number N , for fixed Kondo coupling J and five different couplings g to a sub-Ohmic bosonic bath with $s = 0.2$. Increasing N corresponds to considering the problem on a sequence of exponentially decreasing energy scales [Eq. (3.20)]. The bosonic chain was extended at each even iteration starting at $N = 4$. Figure 3(a) shows the flow for $g = 0$, where the impurity spin and bosonic bath are decoupled. The fixed-point spectrum reached, with effective J infinite, corresponds to that of the regular Kondo model¹⁴ plus a chain of free bosons. The resulting fixed-point Hamiltonian, $H_K^* = \hat{R}^2[H_K^*]$, thus consists of a chain of free bosons and a chain of free fermions described by

$$H_{F,N}^{(L)} = \alpha^{-1} \Lambda^{N/2} \sum_{n=L}^N \epsilon_n f_{n\sigma}^\dagger f_{n,\sigma} + \tau_n (f_{n\sigma}^\dagger f_{n-1,\sigma} + \text{H.c.}). \quad (4.1)$$

with $L = 1$, reflecting the fact that the local moment and conduction electron state at the impurity (f_0) are so strongly coupled — via an infinite Kondo interaction J — that those degrees of freedom are frozen out. Each

TABLE I: Low-lying eigenstates of the even- N fixed-point Hamiltonian H_K^* obtained for $s = 0.2$. The $\{\eta_i^*\}$ denote the limiting eigenvalues of $H_{F,N}^{(1)}$ [Eq. (4.1)] corresponding to the regular Kondo model fixed-point spectrum, while $\{\zeta_i^*\}$ are the limiting eigenvalues for a chain of free bosons.

E	degeneracy	decomposition
0	1	
0.321792450	1	ζ_1^*
0.643584900	1	$2\zeta_1^*$
0.942155004	2	η_1^*
0.965377350	1	$3\zeta_1^*$
1.263947454	2	$\eta_1^* + \zeta_1^*$
1.287169800	1	$4\zeta_1^*$
1.585739904	2	$\eta_1^* + 2\zeta_1^*$
1.608962251	1	$5\zeta_1^*$
1.884310009	4	$2\eta_1^*$
1.907532354	2	$\eta_1^* + 3\zeta_1^*$
1.930754703	1	$6\zeta_1^*$

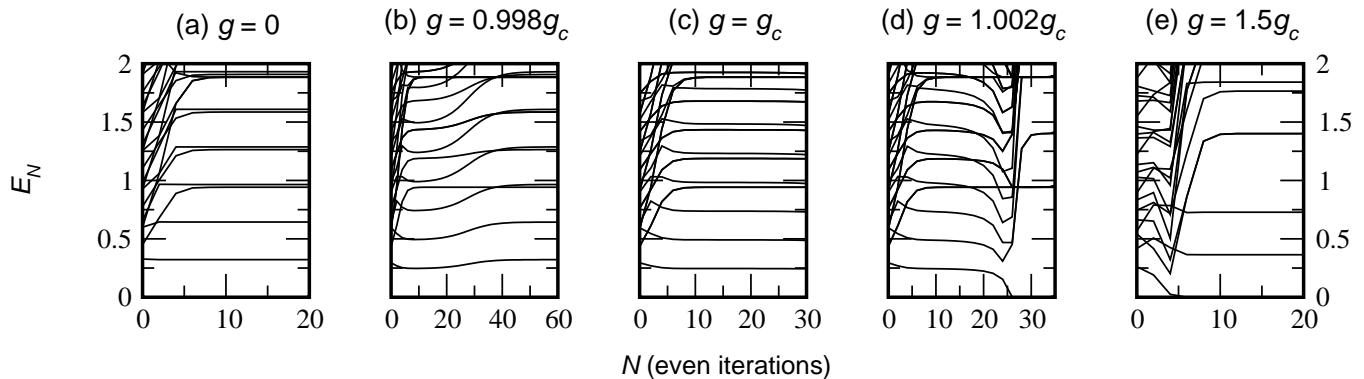


FIG. 3: Low-lying energy levels of H_N as a function of even iteration number N , for bosonic bath exponent $s = 0.2$, Kondo coupling $J = 0.5$ and the values of g shown, with $g_c \simeq 0.567$. The bosonic chain was extended for even N only, as discussed in Sec. III B. (a) Zero coupling to the bosonic bath. (b) For g close to g_c in the Kondo phase, the quantum-critical fixed-point regime [shown in (c)] is accessed for intermediate N (here $10 \lesssim N \lesssim 20$) before the levels flow to the Kondo-phase fixed-point structure (for $N \gtrsim 40$). (d) and (e) In the localized phase, the levels cross over from the critical fixed-point [$10 \lesssim N \lesssim 20$ in (d)] to the localized fixed-point structure observed for large N . The crossover in the flows defines a low-energy scale T_* that vanishes as $g \rightarrow g_c$.

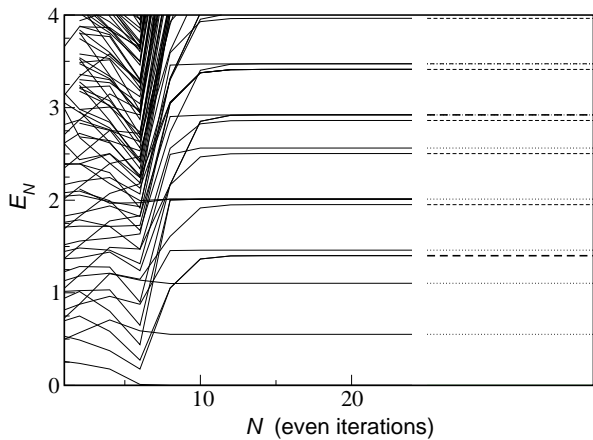


FIG. 4: Interpretation of the low-lying energy levels of the localized fixed-point Hamiltonian H_L^* . The left-hand portion of the figure shows H_N as a function of even iteration number N , for $s = 0.2$, $J = 0.5$, and $g = 0.7$. The spectrum can be decomposed into the product of pure-fermionic and pure-bosonic spectra. Plotted on the right-hand side are the levels listed in Table I, with pure-fermionic excitations shown as dotted lines, pure-bosonic excitations as thick dashed lines, and mixed excitations shown as thin dashed lines.

chain problem can be numerically diagonalized to yield a set of single-particle levels that does not depend on N for $N \gg 1$ (apart from an odd-even alternation for the fermionic case). A decomposition of the lowest lying eigenstates of the even- N Kondo fixed point is provided in Table I.

For all $g < g_c$, the effective bosonic coupling flows to zero [see Fig. 2(a)], while the effective J flows to infinity, and the fixed-point level structure reached for large iteration number N is identical to that for $g = 0$. This is seen clearly in Fig. 3(b). However, for g close to g_c , the flow first approaches an unstable or critical fixed point. This is also clearly observed in Fig. 3(b) for $10 < N < 20$, before the flow crosses over to the stable Kondo fixed point. The low-energy scale set by the crossover from unstable to stable fixed point vanishes as $g \rightarrow g_c$ and is discussed further in Sec. IV C. The level structure for the critical fixed point is shown in Fig. 3(c), obtained for $g \simeq g_c$.

In the localized phase $g > g_c$, the spectrum of the fixed-point Hamiltonian H_L^* can also be decomposed into a product of pure-bosonic and pure-fermionic spectra. Figure 4 shows NRG level flows for $g = 0.7$ and otherwise the same parameters as Fig. 3. Localized-fixed-point behavior is there seen for $N \gtrsim 15$, and the fixed-point spectrum can be decomposed into pure-fermionic excitations, pure-bosonic excitations, and appropriate linear combinations of the two, as shown in Table II. The bosonic spectrum is identical to that of the localized fixed point of the corresponding sub-Ohmic spin-boson model, while the fermionic spectrum corresponds to that of an anisotropic Kondo model in which J_\perp has renormalized to zero [see Fig. 2(a)]. The fixed-point value of J_z is finite for $g > g_c$ and diverges as $g \rightarrow g_c^+$ according to

$$J_z^* \propto (g - g_c)^{-\beta}, \quad (4.2)$$

where β is the magnetic critical exponent defined in Sec. IV D. This behavior is demonstrated in Fig. 5, which shows J_z^* versus $g - g_c$ for $J = 0.5$ and two values of the bosonic bath exponent. In both cases the values of the exponent β agree with those obtained in Sec. IV D to within 2%.

As $s \rightarrow 0^+$ the critical fixed point merges with the

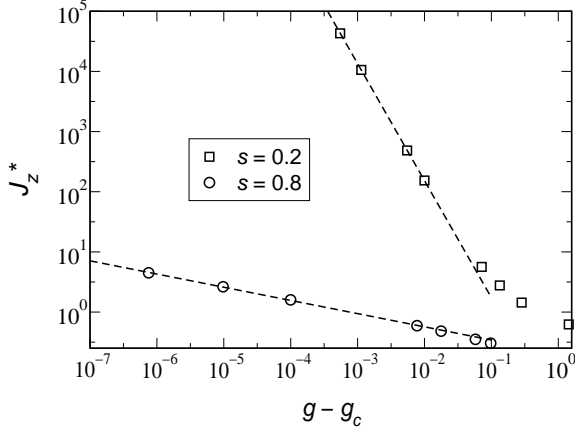


FIG. 5: Effective coupling J_z^* at the localized fixed point for the bath exponents specified in the legend and $J = 0.5$. J_z^* exhibits a power-law divergence as $g \rightarrow g_c^+$ [see Eq. (4.2)]. The values of the exponent β agree with those obtained in Sec. IV D to within 2%.

Kondo fixed point. For any $-1 < s \leq 0$, the critical coupling $g_c(s) = 0$, i.e., the system is localized for any nonzero g . For small g the flow approaches the Kondo fixed point discussed above [shown schematically in Fig. 2(b)], before crossing over to the localized fixed point on an energy scale T_* that vanishes as $g \rightarrow 0$. For $s = 1$

TABLE II: Low-lying eigenstates of the even- N fixed-point Hamiltonian H_L^* , which can be decomposed into the product of a pure bosonic and pure fermionic spectrum. The former, $\{\omega_i^*\}$, is that of the localized fixed point for the spin-boson model and is independent of $g > g_c$. The latter $\{\eta_i^*\}$ correspond to a pure-fermionic anisotropic Kondo model: $J_z^*(g = 0.7) \simeq 2.772$ and $J_\perp^* = 0$. The fixed-point value J_z^* diverges as $g \rightarrow g_c^+$.

E	degeneracy	decomposition
0.000000	2	
0.551499	2	η_1^*
1.102998	2	$2\eta_1^*$
1.400966	2	ω_1^*
1.460443	2	η_2^*
1.952465	2	$\omega_1^* + \eta_1^*$
2.011942	4	$\eta_1^* + \eta_2^*$
2.503964	2	$\omega_1^* + 2\eta_1^*$
2.563441	2	$2\eta_1^* + \eta_2^*$
2.861409	2	$\omega_1^* + \eta_2^*$
2.920886	2	$2\eta_2^*$
2.922716	2	ω_2^*
3.412908	4	$\omega_1^* + \eta_1^* + \eta_2^*$
3.472385	2	$\eta_1^* + 2\eta_2^*$
3.474215	2	$\omega_2^* + \eta_1^*$
3.964407	2	$\omega_1^* + 2\eta_1^* + \eta_2^*$

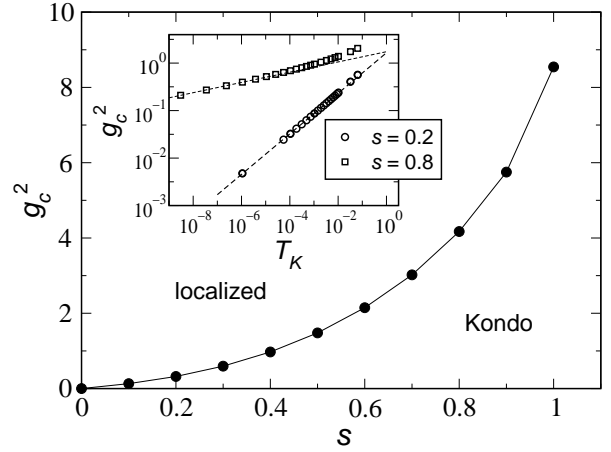


FIG. 6: Critical coupling g_c^2 , separating Kondo and localized phases, versus bosonic bath exponent s for fixed Kondo interaction $J = 0.5$. The inset shows the T_K dependence of g_c^2 for representative bath exponents $s = 0.2$ and 0.8 and the dashed lines are fits to the form $g_c^2 \propto T_K^{1-s}$, which is followed for $T_K \ll 1$. See text for discussion.

the QPT is Kosterlitz-Thouless-like, considered in Sec. V, while for $s > 1$ the Kondo fixed point is reached regardless of the strength of coupling to the bath.

B. Critical coupling

The critical coupling g_c , which marks the phase boundary between Kondo-screened and localized phases for $0 \leq s \leq 1$, is shown in Fig. 6 as a function of bath exponent s . For $s \rightarrow 0^+$, $g_c^2(s)$ vanishes linearly in s . The line of continuous quantum phase transitions for $0 < s < 1$ terminates at the Kosterlitz-Thouless transition point at $s = 1$.

Figure 7 demonstrates, for representative bath exponents $s = 0.2$ and 0.8 , that the critical couplings converge rapidly upon increasing the truncation parameters N_s and N_b , denoting respectively the number of states retained from one NRG iteration to the next and the maximum number of bosons allowed per site of the bosonic chain. In percentage terms, g_c converges with increasing N_b more rapidly for smaller s , but converges with increasing N_s more rapidly for larger s . However, in all cases the choices $N_s = 500$ and $8 < N_b < 12$ are sufficient for the determination of phase boundaries for $\Lambda = 9$. In Sec. IV D we show that critical exponents are also adequately converged for these parameters, a result of crucial importance in judging the success of the approach, and one that is not *a priori* guaranteed.

Of course, deep inside the localized phase it is to be expected that an approach using the lowest $N_b + 1$ eigenstates of $b_M^\dagger b_M$ as basis states for each bosonic site M , will ultimately fail due to a divergence of the mean site-

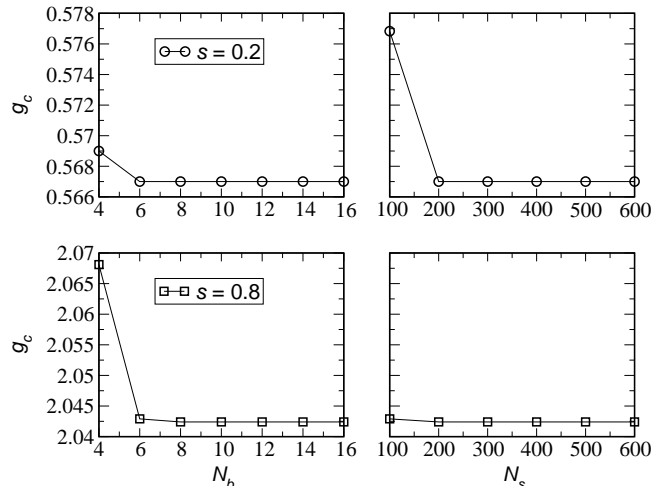


FIG. 7: Dependence of critical coupling g_c on NRG truncation parameters N_b and N_s for $J = 0.5$, NRG discretization $\Lambda = 9$, and bath exponents $s = 0.2$ and $s = 0.8$. The first column demonstrates rapid convergence in N_b for fixed $N_s = 500$. The second column shows convergence in N_s for fixed $N_b = 8$.

occupancy. In a recent study of the SBM using a bosonic NRG approach,^{44,45} Bulla *et al.* have employed a bosonic basis of displaced oscillator states implemented within an alternative “star” formulation of the NRG. While this approach describes well the localized fixed point, it fails to capture correctly both the flow to the delocalized fixed point and the critical properties of primary interest.⁴⁵

The preceding comments are well-illustrated by Fig. 8, which considers the operator for the total number of bosons at iteration N ,

$$\hat{B}_N = \sum_i^{M(N)} b_i^\dagger b_i, \quad (4.3)$$

and its expectation value evaluated at the characteristic temperature T_N , Eq. (3.20). Here, $M(N)$ denotes the highest labelled bosonic site at iteration N . Figure 8 shows $\langle \hat{B}_{20} \rangle$ versus bosonic truncation parameter N_b for both Kondo ($g < g_c$) and localized ($g > g_c$) phases and at the QCP ($g = g_c$) itself. In the Kondo phase and at the QCP, expectation values converge rapidly in N_b , indicating that the lowest eigenstates of H_N are well-described using only the lowest $N_b + 1$ eigenstates of $b_M^\dagger b_M$ as basis states for each bosonic site M . It is clear that no such convergence is achieved inside the localized phase. The difference between the saturated values of $\langle \hat{B}_{20} \rangle$ for critical and delocalized phases is smaller for lower s , consistent with the merging of the critical and delocalized fixed points as $s \rightarrow 0$ (see Fig. 2).

The aim of the present work is to provide a thorough numerical account of the critical behavior of the BFKM. As is demonstrated explicitly in Sec. IV D, the approach

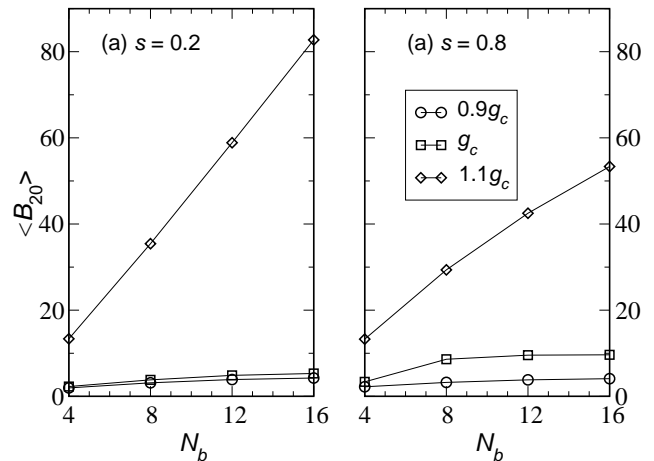


FIG. 8: Dependence of $\langle \hat{B}_{20} \rangle$, defined in text and evaluated at the characteristic temperature scale of iteration $N = 20$, on bosonic truncation parameter N_b for (a) $s = 0.2$ and (b) $s = 0.8$. Data were obtained for $J = 0.5$ and the bosonic couplings g shown in the legend. Convergence with respect to N_b is reached rapidly for $g \leq g_c$.

described in Sec. III provides such a description. We emphasize that critical properties are well-captured regardless of the phase — Kondo *or* localized — from which the critical point is approached.

We now return to a discussion of the phase boundary between Kondo and localized regimes of the model. Reducing J , and hence the Kondo scale T_K of the pure-fermionic ($g = 0$) problem, squeezes out the Kondo-screened phase of the BFKM; specifically, we find

$$g_c^2(s) = c(s) T_K^{1-s} \text{ for } T_K \ll 1, \quad (4.4)$$

with $c(s)$ an s -dependent constant that vanishes both as $s \rightarrow 0^+$ and $s \rightarrow 1^-$, in agreement with perturbative (in $\epsilon \equiv 1 - s$) RG calculations.¹⁷

The form of Eq. (4.4) is demonstrated in the inset to Fig. 6, which shows g_c^2 versus T_K on a logarithmic scale for $s = 0.2$ and 0.8 . Here, we define $T_K \equiv D \exp[-A(\Lambda)/J]$. The Λ -dependent constant $A(\Lambda)$ tends to correct the effects of discretization, which reduce the effective coupling between impurity and band, and leads to the most faithful description of the impurity problem.⁵⁴ The slopes of the linear fits, shown as dashed lines, reveal that the exponent is $1 - s$ to high accuracy, which relation holds for all $0 < s < 1$. We note that this exponent follows from simple dimensional arguments. When all other energy scales in the problem are much smaller than the cut-offs, the problem may be rescaled in terms of T_K , with a single dimensionless parameter $g^2(T_K/\omega_0)^{1-s}$.

If the Kondo scale T_K is recognized as a (renormalized) tunneling amplitude between the two spin states of

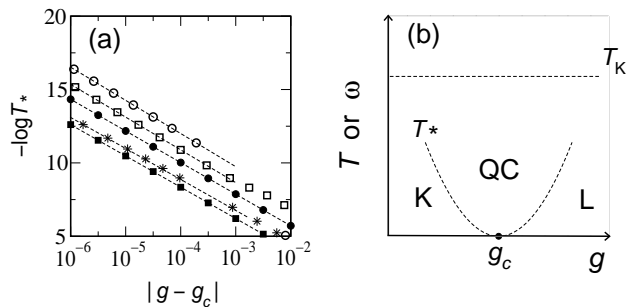


FIG. 9: (a) Power-law behavior of the crossover scale $T_* \propto \Lambda^{-N_*/2}$ in the vicinity of the QCP. Data are shown for $s = 0.5$, $J = 0.5$ (solid symbols) and $J = 0.1$ (open symbols), for both the Kondo (circles) and localized (squares) phases with NRG discretization $\Lambda = 9$. Kondo-phase data obtained for $s = 0.5$, $J = 0.5$, and $\Lambda = 3$ are shown as stars. The correlation-length exponent $\nu(s)$ is universal and is independent of J , of the phase from which the QCP is approached, and of Λ . (b) Schematic crossover diagram valid near the QCP for $0 < s < 1$. The dashed line shows T_* , the scale for crossover between critical and stable fixed-point behavior in static or dynamical quantities. The horizontal dashed line marks T_K , the Kondo scale of the pure-fermionic problem, which serves as a high-energy cutoff for the quantum-critical behavior.

the impurity, then Eq. (4.4) follows from the sub-Ohmic spin-boson model result,⁴⁴ where it is found that the critical dissipation strength $\alpha_c \propto \Delta^{1-s}$ for $\Delta \ll \omega_0$. Such an interpretation follows, of course, from the bosonization discussed in Sec. II B. The sub-Ohmic BFKM can be mapped to a spin-boson model with a sub-Ohmic bath *plus* an Ohmic contribution arising from bosonization of the Kondo part of the Hamiltonian. While the sub-Ohmic behavior dominates the bath spectral function at low energies, and hence determines the universal critical properties, the Ohmic contribution acts to renormalize the bare couplings, as discussed more generally in Ref. 1. Specifically $J \rightarrow T_K$, leading to an effective SBM with $\Delta \propto T_K$ and a sub-Ohmic bath.

C. Crossover scale

We now extract the correlation length exponent ν for the BFKM, considering bath exponents in the range $0 < s < 1$. It is a general feature of a continuous quantum phase transition⁵⁵ that a characteristic energy scale for fluctuations above the ground state vanishes as $g \rightarrow g_c$ with a universal exponent νz . The exponent ν describes the divergence of the spatial correlation length at the critical coupling, and the dynamical exponent z specifies the effective spatial dimensionality of each time dimension. Note that $z = 1$ for impurity models.

Close to the critical coupling g_c , the crossover from the unstable quantum-critical regime to one or other of the stable regimes, defines an energy scale T_* that vanishes precisely at g_c in a fashion governed by the correlation-

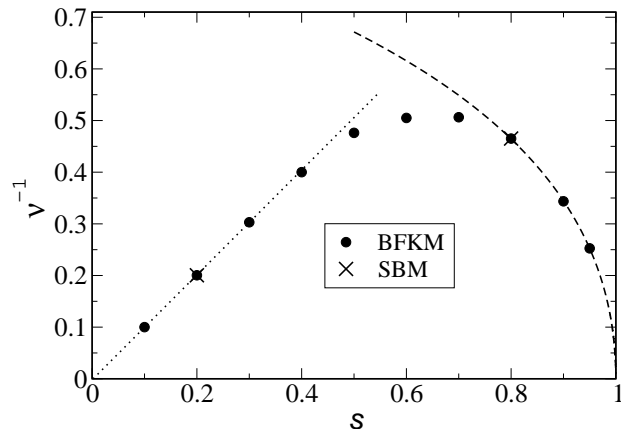


FIG. 10: Dependence of the correlation length exponent $\nu(s)$ on bath exponent s . Results for the spin boson model are plotted as crosses. For $s \rightarrow 0$, $\nu^{-1} \simeq s$ (fit shown as dotted line) while ν^{-1} vanishes as $\sqrt{2(1-s)}$ for $s \rightarrow 1$ (fit shown as dashed line).

length exponent:

$$T_* \propto |g - g_c|^\nu. \quad (4.5)$$

T_*^{-1} sets the time-scale for the decay of the local-moment fluctuations. Close to the QCP the characteristic energy scale in the problem is T_* , while at the QCP itself the only relevant energy scale is the temperature, as discussed in Sec. IV D 2 in the context of ω/T scaling. The crossover scale T_* may be determined directly from the NRG many-body spectrum, via $T_* \propto \Lambda^{-N_*/2}$. Here, N_* is the NRG iteration number at which a selected energy level crosses over from the critical fixed point to a stable fixed point. For example, for the lowest nonzero energy level in Fig. 3(b), the clear crossover from critical ($E_c \simeq 0.246$) to Kondo regime ($E_K \simeq 0.322$) occurs for $N_* \simeq 27.2$, with N_* here defined such that $E_{N_*} = \frac{1}{2}(E_c + E_K)$. Alternatively, T_* may be extracted from crossovers seen directly in properties such as the local static or dynamical susceptibility or the single-particle spectrum. Good agreement is found in all cases to within the numerical uncertainty, which is typically less than 1%.

Fig. 9(a) shows $T_* \propto N_*$ versus $|g - g_c|$ for $J = 0.5$, $s = 0.5$ and a range of couplings g approaching $g_c \simeq 1.22$ from either phase. The form Eq. (4.5) holds well over several orders of magnitude, as reflected in the linear behavior of the data on a logarithmic scale, and any deviations for small $|g - g_c|$ are removed by a more accurate determination of g_c . The correlation-length exponent ν is proportional to the slope of the lines and it is therefore clear to see that ν is independent of Kondo coupling J and the phase (Kondo or localized) from which the

QCP is approached. The exponent is universal, as are all others discussed below, and depends only on the bosonic bath exponent s , which thereby plays the role of a dimension. The insensitivity to Λ is also demonstrated in Fig. 9(a), justifying our choice to work with $\Lambda = 9$ (and hence fewer retained states) for extracting critical exponents.

The behavior shown in Fig. 9(a) is representative of that for all s in the range $0 < s < 1$. A generic crossover diagram is shown in Fig. 9(b), valid in the vicinity of the QCP and for T (and ω) below a nonuniversal cutoff scale (above which free-local-moment behavior obtains). For $T < T_*$, behavior characteristic of either the Kondo ($g < g_c$) or the localized ($g > g_c$) phase is observed, while for $T > T_*$ behavior characteristic of the QCP itself obtains. At the QCP, where $T_* = 0$, the latter behavior persists right down to $T = 0$. This results in the familiar picture for a quantum phase transition of quantum-critical behavior emanating from a singular point at $T = 0$ and influencing a large part of the phase diagram in the g - T (or g - ω) plane. Such a picture has emerged in recent years in a number of quantum impurity problems.¹⁹

The dependence of ν on the continuous parameter (dimension) s is shown in Fig. 10(a). For both $s \rightarrow 0^+$ and $s \rightarrow 1^-$ the correlation length exponent diverges, which reflects the qualitative changes occurring at these critical dimensions, as described above. For small s ,

$$\nu(s) \simeq 1/s, \quad (4.6)$$

which result holds reasonably well for $s = 0.4$, and becomes asymptotically exact as $s \rightarrow 0^+$ [see dotted line fit in Fig. 10(a)]. For $s \rightarrow 1$ the exponent approaches

$$\nu(s) \simeq 1/\sqrt{2(1-s)} + C, \quad (4.7)$$

with $C \simeq 0.4$, which fit is shown as the dashed line in Fig. 10(a). Most importantly, we demonstrate that the correlation length exponents of this Ising anisotropic BFKM are in essentially exact agreement with those of the spin-boson model obtained in Refs. 44 and 48. This is true for all exponents calculated, providing numerical confirmation that the quantum-critical points of the two models belong to the same universality class — an equivalence implied by the bosonization treatment discussed in Sec. II B.

The results $\nu(s) \simeq 1/s$ and $g_c^2/T_K \propto s$ as $s \rightarrow 0$ [Eqs. (4.6) and (4.4) respectively] imply a form for the vanishing of the crossover scale T_* at $s = 0$. Here the system is always localized for any $g > 0$ and we predict that T_* , describing the direct crossover from Kondo to localized behavior, vanishes approaching $g = g_c = 0$ as

$$\ln T_* \propto -\frac{T_K}{g^2}, \quad \text{for } s = 0. \quad (4.8)$$

This is confirmed numerically in Fig. 11, which shows data for $J = 0.5$ rescaled according to Eq. (4.8). The dashed line shows a linear fit for $g^2 \ll 1$. The inset demonstrates that the slope of the fit is proportional to

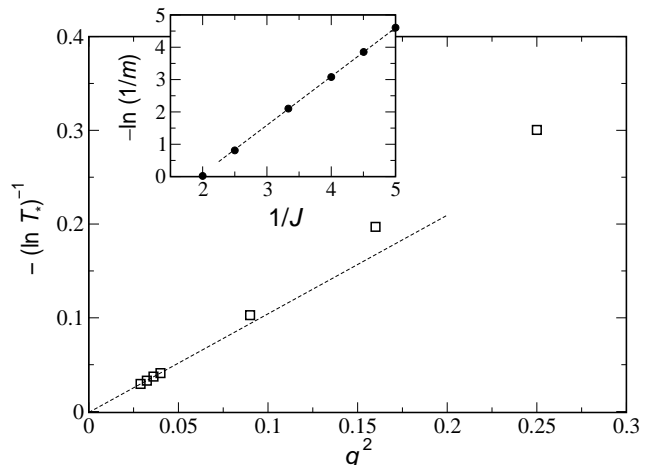


FIG. 11: Crossover scale for $s = 0$ vanishing as Eq. (4.8) for $g \rightarrow 0$. The data in the main figure were obtained for $J = 0.5$. A linear fit to the data points at lowest g^2 is shown as a dashed line. The inset demonstrates that the slope m of the fit varies as $1/T_K$ — see text.

T_K^{-1} , where $T_K \equiv D \exp[-A(\Lambda)/J]$. For the sub-Ohmic spin-boson model, identifying $\Delta \propto T_K$ and $\alpha \propto g^2$ leads to $\ln T_* \propto (-\Delta/\alpha)$ for $s = 0$, which result has also been obtained via a perturbative RG analysis.⁴⁸

D. Local magnetic response

The local susceptibility, $\chi_{\text{loc}}(\omega) = \chi'_{\text{loc}}(\omega) + i\chi''_{\text{loc}}(\omega)$, is defined as

$$\chi_{\text{loc}}(\omega) = i \int_0^\infty e^{-i\omega t} \langle [S_z(t), S_z(0)] \rangle \quad (4.9)$$

with $\chi'_{\text{loc}}(\omega = 0)$ being the static response

$$\chi_{\text{loc}}(0) = - \left. \frac{\partial \langle S_z \rangle}{\partial h} \right|_{h=0} = \lim_{h \rightarrow 0} - \frac{\langle S_z \rangle}{h} \quad (4.10)$$

to a local magnetic field h acting only at the impurity site through an additional term in the Hamiltonian $\Delta \hat{H} = h S_z$ (setting $g\mu_B \equiv 1$).

In the present section we focus on the sub-Ohmic case with $0 < s < 1$. The case of Ohmic dissipation, $s = 1$, is discussed separately in Sec. V. In Sec. IV D 1 we consider the local static susceptibility $\chi_{\text{loc}}(T; \omega = 0)$ calculated by evaluating the right-hand side of Eq. (4.10) directly for small fields in the range $10^{-12} \leq h \leq 10^{-8}$. We extract various critical exponents for the transition which are shown to satisfy hyperscaling relations characteristic of an interacting quantum-critical point. We calculate the dynamical local susceptibility in Sec. IV D 2 which obeys ω/T scaling in the vicinity of the QCP. We reiterate that all results presented are converged with respect

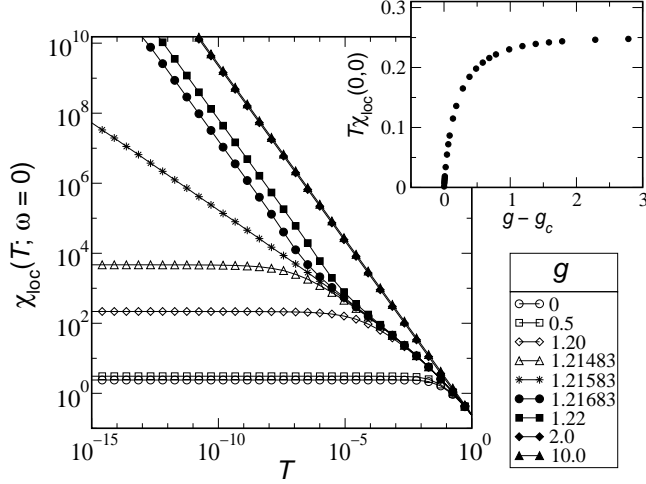


FIG. 12: Static local susceptibility $\chi_{\text{loc}}(T; \omega = 0)$ versus T for $s = 0.5$, $\rho_0 J = 0.5$ and different g , where $g_c \simeq 1.21583$. $\chi_{\text{loc}}(0, 0) = 0$ for $g < g_c$. At the critical coupling we find $\chi_{\text{loc}}(T; 0) \propto T^{-x}$ with $x = 0.500(2)$. The inset shows the vanishing of $T\chi_{\text{loc}}(0, 0)$ for $g \rightarrow g_c^+$. Analogous data for $s = 0.2$ are shown in Fig. 2 of Ref. 46.

to the truncation parameters N_b and N_s . For the data discussed, $N_b = 8$ and $N_s = 500$ are sufficient to converge critical exponents to the required accuracy — see, e.g., Fig. 13.

1. Static susceptibility

The Kondo and localized phases are readily distinguished by the limiting low-temperature behavior of $\chi_{\text{loc}}(T; \omega = 0)$. If a local moment $M_{\text{loc}} \equiv \langle S_z \rangle$ exists at the impurity site for $T \rightarrow 0$, then

$$\chi_{\text{loc}}(T; \omega = 0) = \frac{M_{\text{loc}}(0)^2}{T} \text{ for } T \ll T_*. \quad (4.11)$$

We find such behavior for $g > g_c$, as shown in Fig. 12.

For $g \gg g_c$ the residual moment $M_{\text{loc}}(0)$ approaches the value for a completely decoupled spin, $M_{\text{loc}}(0)^2 = S(S+1)/3$, as seen clearly in the inset to Fig. 12. For $0 < s < 1$, the low-temperature limit of $T\chi_{\text{loc}}(g > g_c, T; \omega = 0)$ vanishes continuously at the QCP, viz

$$\lim_{T \rightarrow 0} T\chi_{\text{loc}}(g > g_c, T; \omega = 0) \propto (g - g_c)^\lambda, \quad (4.12)$$

as is also clear from the inset to Fig. 12. Equations (4.11) and (4.12) imply that

$$M_{\text{loc}}(g > g_c; T = 0) \propto (g - g_c)^\beta \quad (4.13)$$

with $\beta = \lambda/2$.

For $g < g_c$, by contrast, we find the characteristic signature of a screened ground state with quenched impurity

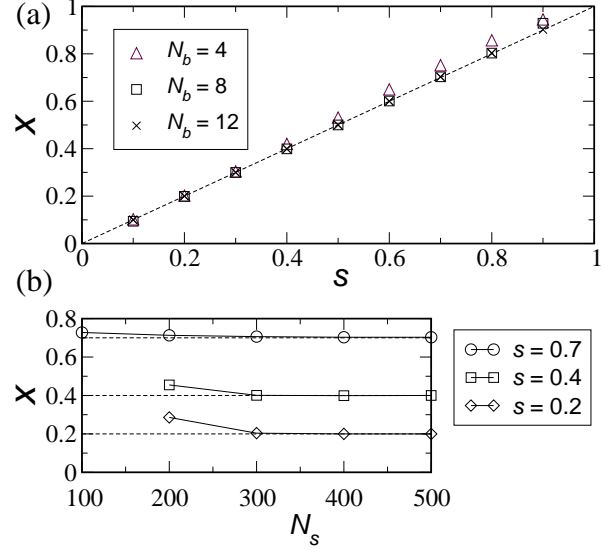


FIG. 13: Dependence of the critical exponent x , as defined in Eq. (4.16), on bath exponent s in the range $0 < s < 1$. The data were obtained for Kondo coupling $J = 0.5$, discretization parameter $\Lambda = 9$, and (a) $N_s = 500$, (b) $N_b = 12$. The dotted lines show $x = s$.

degrees of freedom (as exists ubiquitously in the regular Kondo model):

$$\chi_{\text{loc}}(T; \omega = 0) = \text{const.} \quad \text{for } T \ll T_*, \quad (4.14)$$

which behavior is also seen clearly in Fig. 12. For $0 < s < 1$ it is found that

$$\chi_{\text{loc}}(g < g_c; T = 0, \omega = 0) \propto (g_c - g)^{-\gamma}, \quad (4.15)$$

signalling a collapse of the Kondo effect at $g = g_c$ (see Fig. 14) discussed further below.

At the QCP itself, $g = g_c$, we find the anomalous behavior

$$\chi_{\text{loc}}(T; \omega = 0, g = g_c) \propto T^{-x}. \quad (4.16)$$

To high accuracy we find

$$x = s \quad (4.17)$$

for $0 < s < 1$, confirming the prediction of ϵ -expansion studies^{17,18} that $x = s$ to all orders in $\epsilon \equiv 1 - s$. The result Eq. (4.17) has also recently been reported for the sub-Ohmic spin-boson model.^{44,48} We note in passing that since the total spin quantum number is not conserved in the BFKM, the impurity contribution to the total susceptibility χ_{imp} also acquires an anomalous exponent at criticality. Again, we find $\chi_{\text{imp}}(T) \propto T^{-s}$.

For $T \ll T_K$ the local static susceptibility obeys the scaling form

$$T_K \chi_{\text{loc}}(T; \omega = 0) = \left(\frac{T_*}{T_K} \right)^{-s} \bar{\phi}_{s,p} \left(\frac{T}{T_*} \right) \quad (4.18)$$

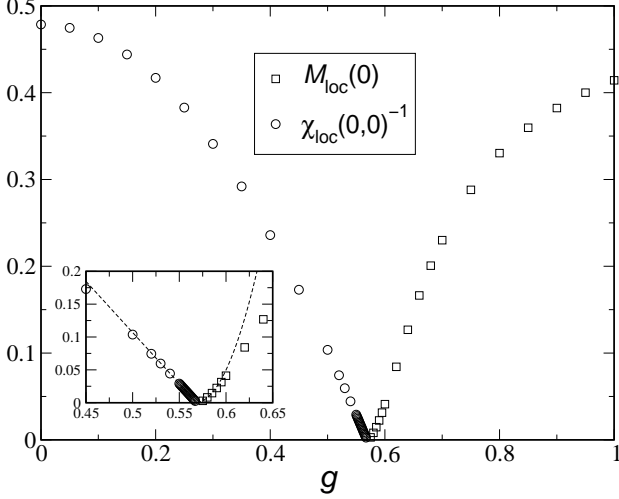


FIG. 14: Order parameter $M_{\text{loc}}(g > g_c; T = 0)$ and renormalized Kondo temperature $\chi_{\text{loc}}(g < g_c; T = 0, \omega = 0)^{-1}$ versus bosonic coupling g , for $s = 0.2$ and $J = 0.5$. Both quantities vanish continuously for $g \rightarrow g_c$. The inset shows fits (dashed lines) for small $|g - g_c|$. See text for discussion.

where $\bar{\phi}_{s,p}$ is a universal function and $p = K$ or L denotes the phase. For $z \gg 1$, $\bar{\phi}_{s,p}(z) \propto z^{-s}$ and $T_K \chi_{\text{loc}}(T) \propto (T/T_K)^{-s}$ is independent of T_* .

Before proceeding we illustrate the convergence of the critical exponents in the NRG truncation parameters N_b and N_s , which denote respectively the maximum number of bosons allowed per site of the bosonic chain and the maximum number of states retained from one NRG iteration to the next. The behavior of the critical exponent x is typical and is shown in Fig. 13 as a function of bosonic bath exponent s . Figure 13(a) shows data obtained for $N_b = 4, 8$ and 12 , each converged with respect to N_s , the number of states retained. Upon increasing N_b , the exponent x is found to approach $x = s$ [dashed line in Fig. 13(a)] for all s , the convergence being faster for small s . For this and all other critical exponents calculated we find that by $8 < N_b < 12$ sufficient convergence is achieved. Figure 13(b) illustrates the dependence of x on the number of states retained N_s , calculated for $N_b = 12$ and three values of s . The exponent converges rapidly with increasing N_s , approaching $x = s$ (dashed lines) in each case. In summary, we find that by $N_b = 12$ and $N_s = 500$ the critical exponent x is converged to within 1% of $x = s$ for all s examined in the range $0 < s < 1$. The observation that fewer bosons are required to achieve convergence for $s \ll 1$ is consistent with the merging of the critical and delocalized fixed points as $s \rightarrow 0$.

We now return to a discussion of the various critical exponents introduced above, for which similar convergence is observed. The vanishing as $g \rightarrow g_c^+$ of the residual moment $M_{\text{loc}}(T = 0)$, which serves as the order parameter for the problem, is shown in Fig. 14 (squares). This pic-

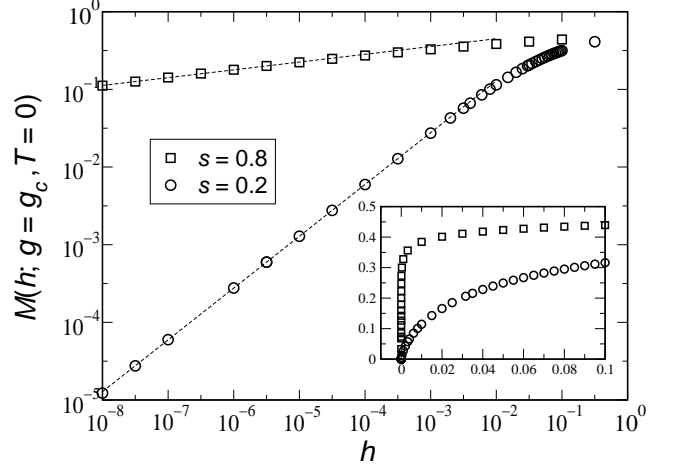


FIG. 15: Dependence of residual moment $M_{\text{loc}}(g = g_c, T = 0)$ on local magnetic field h , for $J = 0.5$. The dashed lines are fits to the data, as discussed in the text. The inset shows the data on an absolute scale.

ture remains qualitatively valid for all bath exponents in the range $0 < s < 1$. For the specific case $s = 0.2$ shown, the exponent defined in Eq. (4.13) is $\beta \equiv \frac{1}{2}\lambda \simeq 1.99(2)$, with the estimated numerical uncertainty in the last digit given in parentheses. The fit is shown as a dashed line in the inset to Fig. 14. Also shown in Fig. 14 is the vanishing of $\chi_{\text{loc}}(g < g_c; T = 0, \omega = 0)$ for $g \rightarrow g_c^-$ described by exponent γ [Eq. (4.15)]. $\chi_{\text{loc}}(0, 0)^{-1}$ measures the Kondo temperature, which is strongly renormalized due to the competing coupling to the dissipative bosonic bath, and its vanishing as $g \rightarrow g_c^-$ signals criticality in the Kondo screening. For $s = 0.2$, $\gamma \simeq 1.00(1)$, and the dotted line in the inset shows a linear fit to the $g \rightarrow g_c^-$ data points.

The dependence of $M_{\text{loc}}(h; g = g_c, T = 0)$ on the local field h defines the magnetic critical exponent δ :

$$M_{\text{loc}}(h; g = g_c, T = 0) \propto |h|^{\frac{1}{\delta}}. \quad (4.19)$$

Figure 15 shows data obtained for $J = 0.5$ and $g = g_c$ for both $s = 0.2$ and $s = 0.8$; the inset shows the data on an absolute scale, while the main figure reveals the power-law behavior that is observed over several orders of magnitude. The dashed lines are fits to the $h \leq 10^{-3}$ data, of the form of Eq. (4.19), with $1/\delta \simeq 0.665(5)$ [0.106(2)] for $s = 0.2$ [0.8].

Hyperscaling relations among the various critical exponents may be deduced starting from the following scaling ansatz for the critical part of the free energy, which assumes that the fixed point is interacting:

$$F_{\text{crit}} = Tf(|g - g_c|/T^{\frac{1}{\nu}}, |h|/T^b). \quad (4.20)$$

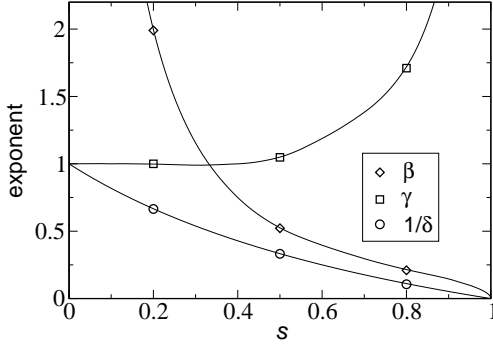


FIG. 16: Behavior of critical exponents β , γ and $1/\delta$ as a function of bosonic bath exponent s in the range $0 < s < 1$. The symbols correspond to directly calculated exponents, while the solid lines were obtained from hyperscaling relations [Eqs. (4.23)] using numerical results for $x(s)$ and $\nu(s)$. Hyperscaling relations are obeyed to within numerical accuracy for all s considered in the range $0 < s < 1$.

Using the standard thermodynamic relations

$$M_{\text{loc}} = -\frac{\partial F_{\text{crit}}}{\partial h}, \quad (4.21)$$

$$\chi_{\text{loc}}(T; \omega = 0) = -\frac{\partial^2 F_{\text{crit}}}{\partial h^2}, \quad (4.22)$$

it readily follows that there are only two independent exponents, i.e.,

$$\delta = \frac{1+x}{1-x}, \quad (4.23a)$$

$$\lambda \equiv 2\beta = \nu(1-x), \quad (4.23b)$$

$$\gamma = \nu x. \quad (4.23c)$$

We find that our numerically determined exponents for $0 < s < 1$ obey these relations to high accuracy, as demonstrated in Fig. 16 which compares numerical obtained exponents β , γ and $1/\delta$ to values predicted by hyperscaling relations. Numerical values for representative cases are given in Table 1 of Ref. 46. It follows from the relations Eqs. (4.23) and the asymptotic results Eqs. (4.6) and (4.7) that for $s \rightarrow 0^+$, $1/\delta \simeq 1 - 2s$, $\lambda \simeq 1/s$ and $\gamma \simeq 1$, while for $s \rightarrow 1^-$, $1/\delta \simeq \frac{1}{2}(1-s)$, $\lambda \propto \sqrt{1-s}$ and $\gamma \propto 1/\sqrt{1-s}$.

We now turn briefly to the regime $-1 < s \leq 0$ through-out which the system is in the localized phase for any $g > 0$. Figure 17 shows the static local susceptibility $\chi_{\text{loc}}(T; \omega = 0)$ versus T for bath exponents $s = 0$ and $s = -0.8$. The observed behavior is typical of any s in the range $-1 < 0 \leq 0$. As indicated by the flow diagram Fig. 2(b), the $g = 0$ (Kondo) spectrum is followed down to progressively lower temperatures as $g \rightarrow 0$ before crossing over directly to localized Curie-like behavior, Eq. (4.11). Consequently, for $T_* \ll T_K$, $\chi_{\text{loc}}(T; \omega = 0)$ obeys the simple scaling form

$$T_K \chi_{\text{loc}}(T; \omega = 0) = \phi_{s,L} \left(\frac{T}{T_*} \right) \quad (4.24)$$

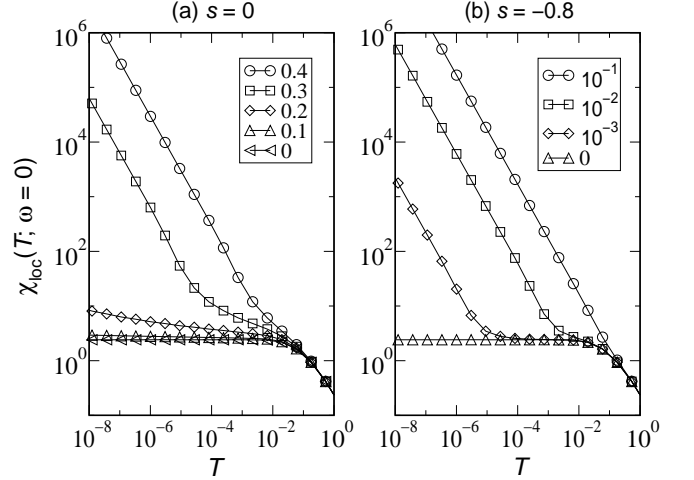


FIG. 17: Static local susceptibility $\chi_{\text{loc}}(T; \omega = 0)$ versus T for $J = 0.5$ and (a) $s = 0$ and (b) $s = -0.8$. The legends refer to the bosonic coupling g . Qualitatively similar behavior is observed in either case: as $g \rightarrow 0$ there is a direct crossover from $g = 0$ Kondo behavior for $T \gg T_*$, to localized Curie-like behavior for $T \ll T_*$. The localized-phase crossover scale T_* vanishes as $g \rightarrow 0$ — see Fig. 18.

with no T_* -dependent prefactor, and $\nu = \lambda$. Figure 18 shows $M_{\text{loc}}(0)^2$ as a function of g^2 for the s values specified. In all cases we find that $M_{\text{loc}}(0)^2$ vanishes continuously with

$$M_{\text{loc}}(0)^2 \propto (g^2)^\lambda. \quad (4.25)$$

The inset plots the inverse of the exponent λ versus bath exponent s . We find $\lambda = \nu \simeq 1/s$ as $s \rightarrow 0^-$, as found for $s \rightarrow 0^+$ (see Fig. 10).

2. Dynamical susceptibility

The local dynamical susceptibility $\chi_{\text{loc}}(\omega)$ can be computed using the NRG via its imaginary part

$$\chi_{\text{loc}}''(\omega) = \frac{\pi}{Z} \sum_{m,n} |\langle n | S_z | m \rangle|^2 (e^{-\beta E_n} - e^{-\beta E_m}) \delta(\omega - E_{nm}), \quad (4.26)$$

with $\chi_{\text{loc}}''(\omega) = \chi_{\text{loc}}''(-\omega)$, $E_{nm} = E_n - E_m$, and $Z = \sum_m e^{-\beta E_m}$ being the partition function. For $T = 0$,

$$\chi_{\text{loc}}''(\omega) = \frac{\pi}{Z_0} \sum_n |\langle n | S_z | 0 \rangle|^2 \delta(|\omega| - E_{n0}) \text{sgn}(\omega) \quad (4.27)$$

with an implicit summation over ground states $|0\rangle$ in cases where the degeneracy $Z_0 > 1$. Because only a small fraction of states are kept from one NRG iteration to the next, it is iteration N that contains the most appropriate information for dynamics at energy scales $D\Lambda^{-N/2}$.

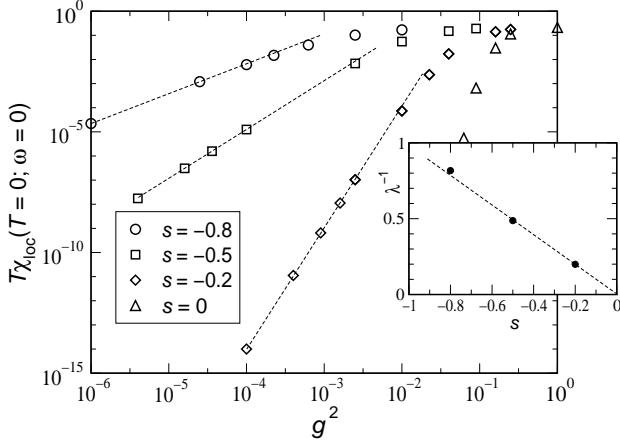


FIG. 18: $M_{\text{loc}}(T=0)^2 = \lim_{T \rightarrow 0} T\chi_{\text{loc}}(T; \omega=0)$ versus bosonic coupling g^2 for the $s \leq 0$ bath exponents specified in the legend. For $-1 < s \leq 0$ the system is always localized for any $g > 0$ and $M_{\text{loc}}(T=0)^2$ is found to vanish continuously as $g \rightarrow 0$. For $g^2 \ll 1$ the data can be fit to the form $M_{\text{loc}}(T=0)^2 \propto (g^2)^\lambda$. The inset shows the exponent λ versus s , which diverges as $\lambda \simeq 1/s$ for $s \rightarrow 0^-$. See text for discussion.

Thus Eq. (4.26) is evaluated at each NRG iteration for a frequency window spanning $\omega_N = \alpha D\Lambda^{-N/2}$. The result is a discrete set of delta-function peaks that must be broadened to recover a continuous spectrum. We follow well-established procedure,⁵⁶ applying Gaussian broadening on a logarithmic scale, viz

$$\delta(\omega - \omega_n) \rightarrow \frac{e^{-b^2/4}}{\sqrt{\pi}b\omega_n} \exp\left[-\frac{(\ln \omega - \ln \omega_n)^2}{b^2}\right], \quad (4.28)$$

taking the broadening parameter $0.3 < b < 0.5$. The static local susceptibility (considered in Sec. IVD 1) follows via Hilbert transformation as

$$\chi_{\text{loc}}(T; \omega=0) = \int_{-\infty}^{\infty} \frac{d\epsilon}{\pi} \frac{\chi_{\text{loc}}''(\epsilon, T)}{\epsilon}. \quad (4.29)$$

Zero temperature. — Figure 19 shows $\chi_{\text{loc}}''(\omega)$ at $T=0$ on a logarithmic scale for a sequence of increasing couplings $g < g_c$. For zero coupling to the bosonic bath, the familiar Kondo-model result obtains: $\chi_{\text{loc}}''(\omega) \propto \omega$ for $\omega \ll T_K$. However, for any nonzero g in the Kondo phase, $\chi_{\text{loc}}''(\omega) \propto \omega^s$ as $\omega \rightarrow 0$, corresponding to power-law relaxation $\chi_{\text{loc}}(t) \propto t^{-(1+s)}$ for long times.

At the QCP ($g = g_c$) we find the scale-free form

$$T_K \chi_{\text{loc}}''(\omega; g = g_c, T=0) \propto \left(\frac{\omega}{T_K}\right)^{-y} \text{sgn}(\omega), \quad (4.30)$$

for $\omega \ll T_K$, with

$$y = x = s \quad (4.31)$$

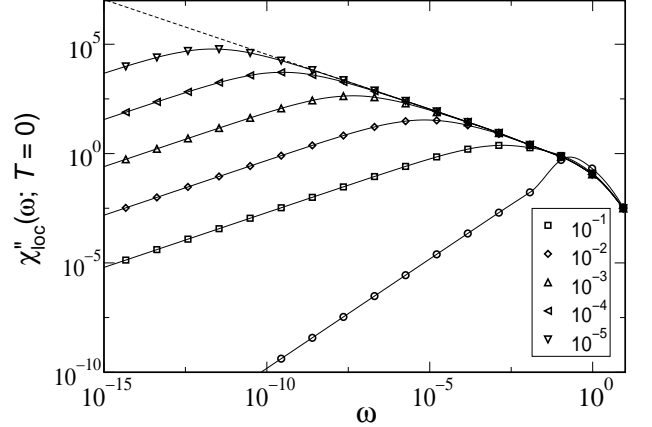


FIG. 19: Imaginary part of the local dynamical susceptibility $\chi_{\text{loc}}''(\omega; T=0)$ for bosonic bath exponent $s = 0.5$, Kondo coupling $J = 0.5$ and a range of $g < g_c \simeq 1.216$ in the Kondo-screened phase. The circles correspond to $g = 0$ while the legend specifies $g_c - g$ for the remaining data. As $g \rightarrow g_c^-$ the curves follow the quantum-critical form for $T_* \ll \omega \ll T_K$. The dashed line is a fit to the latter [Eq. (4.30)] which yields an exponent $y = s$ to within less than 0.5%. See text for further comments.

obeyed for all $0 < s < 1$ to within our estimated numerical error, which is typically less than 1%. This is illustrated in Fig. 20, where $\chi_{\text{loc}}(T; \omega=0)$ and $\chi_{\text{loc}}''(\omega; T=0)$ are plotted on a logarithmic scale for bath exponents $s = 0.2$ and $s = 0.8$, and $g = g_c$ in either case. The result $x = y$ is reflected in the equality of the slopes of the fits (shown as dashed lines).

For small deviations from $g = g_c$ the critical power law behavior is cut off below a crossover scale T^* that vanishes at the QCP according to Eq. (4.5). Thus, the correlation length exponent ν can also be extracted from $\chi_{\text{loc}}''(\omega; T=0)$ and agrees with the results of Fig. 10 to within our estimated numerical error. In the vicinity of the QCP we find the zero-temperature scaling form

$$T_K \chi_{\text{loc}}''(\omega; T=0) = \left(\frac{T_*}{T_K}\right)^{-s} \phi_{s,p}\left(\frac{\omega}{T_*}\right) \quad (4.32)$$

for $T_* \ll T_K$, where $p = K$ or L denotes the phase. For $z \gg 1$, $\phi_{s,p}(z) = z^{-s}$ for either phase and thus $\chi_{\text{loc}}''(\omega)$ is independent of T_* for $\omega \gg T_*$ (see, e.g., Fig. 19), following the quantum-critical form $T_K \chi_{\text{loc}}(\omega) \propto (\omega/T_K)^{-s}$ before ultimately being cut off by the nonuniversal scale T_K/T_* . Such scaling behavior is clearly illustrated in Fig. 21, which shows scaling for $g \rightarrow g_c^-$.

Finite temperature. — The result $y = x$ implies that the relaxation rate is linear in temperature, characteristic of critical physics below the upper critical dimension. Quantum-critical fluctuations are cut off on a timescale

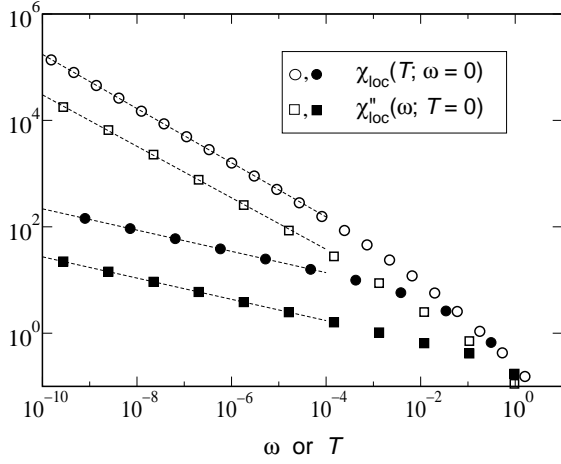


FIG. 20: Critical $\chi''_{\text{loc}}(\omega; g = g_c, T = 0)$ versus ω [$\chi_{\text{loc}}(T; g = g_c, \omega = 0)$ versus T] for $J = 0.5$ and $s = 0.2$ (filled symbols) and $s = 0.5$ (open symbols). It is seen clearly from the equality of the slopes that the exponent $y = x$. Dashed lines are fits to the data and yield exponents $y = x = s$ to within the estimated numerical uncertainty.

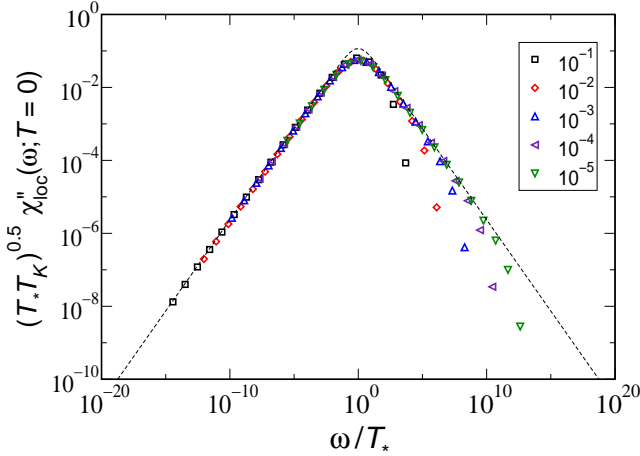


FIG. 21: (Color online) Scaling of the $T = 0$ dynamical susceptibility for $s=0.5$ and $g \rightarrow g_c^-$ — see Eq. (4.32). The data were obtained for $J = 0.5$. The legend specifies $g_c - g$ and T_* is here defined as the location of the peak maximum in Fig. 19, marking the crossover from quantum-critical ω^{-s} behavior for $\omega \gg T_*$ to ω^s for $\omega \ll T_*$. For the data presented, T_* varies over ten orders of magnitude. Excellent data collapse is observed up to scales set by the bare Kondo temperature T_K/T_* . The dashed line is a simple fit taking $\phi_{s,K}(z) \propto z^s/(1+z^{2s})$, which does remarkably well at capturing the entire scaling curve.

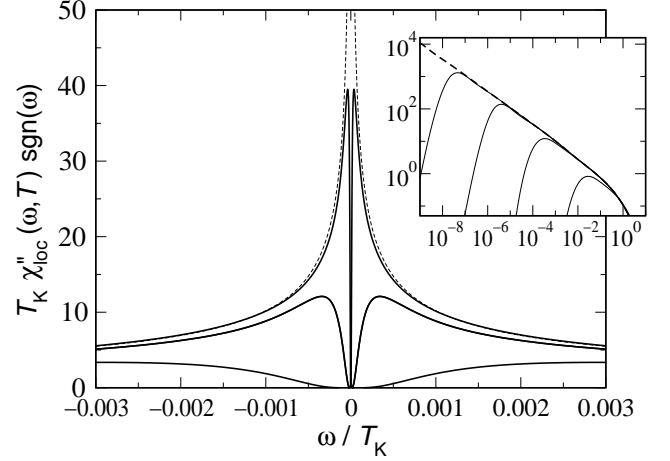


FIG. 22: Imaginary part of the dynamical local susceptibility $\chi''_{\text{loc}}(\omega, T)$ versus ω , at the critical coupling $g = g_c$ for $s = 0.5$ and a sequence of increasing temperatures $T/T_K = 0$ (dotted line), 10^{-5} , 10^{-4} and 10^{-3} . Temperature is the single low-energy scale, setting the location of the peak maximum. The inset shows data on a logarithmic scale for $T/T_K = 10^{-2}$, 10^{-4} , 10^{-6} and 10^{-8} . The $T = 0$ data are shown as a dashed line and follow the critical power law Eq. (4.30) with $y = 0.5$.

$\tau = \hbar/k_B T$. Thus, for nonzero $T \ll T_K$ the quantum-critical form Eq. (4.30) is cut off for frequencies $\omega \approx T$, as is shown clearly in the inset to Fig. 22. For $\omega/T \ll T_K/T$ this leads to ω/T scaling of the form

$$T_K \chi''_{\text{loc}}(\omega, T; g = g_c) = \left(\frac{T}{T_K}\right)^{-s} \phi_s\left(\frac{\omega}{T}\right). \quad (4.33)$$

with $\phi_s(z) = z^{-s}$ for $z \gg 1$. The numerically obtained QCP scaling curve is shown in Fig. 23 as the thick line. Though the NRG method is unreliable for $\omega \lesssim T$ (Refs. 52 and 57) due to truncation error, we find a consistent description of the finite- T scaling properties of the model as discussed further below. See also Fig. 3 of Ref. 46, which demonstrates ω/T scaling for $s = 0.2$ and different values of T_K .

For any finite T_* , the local dynamical susceptibility obeys the full scaling form to be expected in the vicinity of an interacting QCP¹⁹:

$$T_K \chi''_{\text{loc}}(\omega, T) = \left(\frac{T}{T_K}\right)^{-s} \Phi_{s,p}\left(\frac{\omega}{T}, \frac{T_*}{T}\right). \quad (4.34)$$

Figure 23 plots ω/T scaling curves obtained via NRG calculations for several values of the ratio T_*/T in the Kondo-screened phase of the model for $s = 0.5$. For $\omega/T \gg T_*/T$ the curves follow the QCP ($T_* = 0$) form [Eq. (4.33)], which is of course independent of phase, $p = K$ or L . Clearly, as $T_*/T \rightarrow 0$ the curves follow the QCP result more closely, i.e., $\phi_s(z) = \Phi_{s,p}(z, 0)$.

E. Spectral function

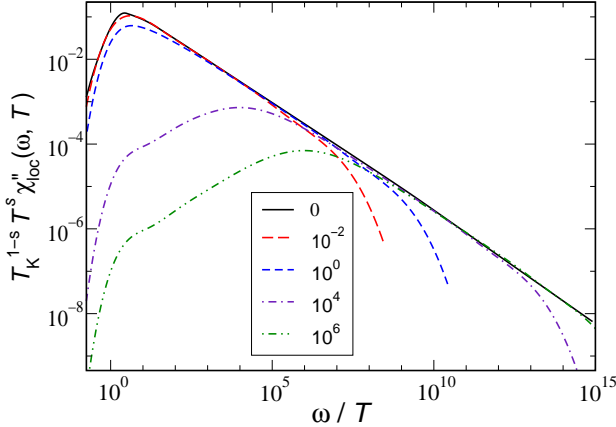


FIG. 23: (Color online) ω/T scaling of the dynamical local susceptibility in the Kondo phase for $s = 0.5$ and values of T_*/T specified in the legend. The QCP spectrum obtains for $T_*/T = 0$. The tails of the curves fall onto the QCP form for $T_*/T \ll \omega/T \ll T_K/T$, as shown clearly by the $T_*/T = 10^6$ data. Here, T_* is defined as the crossover scale in $\chi''_{loc}(\omega; T = 0)$ from ω^{-s} to ω^s behavior.

For the opposite extreme $T_*/T \rightarrow \infty$, the $T = 0$ result obtains when suitably rescaled (see Fig. 21), such that $\Phi_{s,p}(z', z) = z^{-s} \phi_{s,p}(z'/z)$ for $z, z' \rightarrow \infty$. Since all data were obtained for finite T_K , the tail behavior is ultimately cut off when ω/T increases to scales of order T_K/T , as seen in the figure. The T_*/T dependence of the ω/T scaling spectrum has also been discussed in the context of the Kondo model with a pseudogap host density of states $\rho(\epsilon) \propto |\epsilon|^r$, though the QCP of the latter model belongs to a different universality class.^{58,59}

To summarize this subsection, we have studied in detail the local magnetic response for the Ising-anisotropic BFKM, extracting a range of critical exponents. For $0 < s < 1$ we find that the exponents satisfy hyperscaling relations and ω/T -scaling characteristic of an interacting critical fixed point. All exponents associated with the local magnetic susceptibility can be determined by knowledge of just x and ν . Furthermore, we find excellent agreement with corresponding results for the spin-boson model, confirming that the two models belong to the same universality class. As pointed out in Ref. 48, these results demonstrate the failure of a mapping^{60,61} of the SBM to a one-dimensional classical Ising model with long-range interactions falling off as $1/r^{1+s}$. The latter model is above its upper critical dimension for $0 < s < \frac{1}{2}$ and the exponents there take mean-field values with hyperscaling relations violated. However, in the range $\frac{1}{2} < s < 1$ the SBM and classical long-range Ising model appear to be equivalent. See Refs. 48 and 19 for further discussion of this issue.

We now turn to a discussion of the local single-particle spectrum, paying particular attention to the destruction of the Kondo resonance at the quantum-critical point. In this section we calculate the impurity spectral function

$$A(\omega) = \frac{1}{Z} \sum_{n,m} |\langle n | d_\sigma^\dagger | m \rangle|^2 \delta(\omega - E_{n,m}) (e^{-\beta E_m} + e^{-\beta E_n}) \quad (4.35)$$

for the Ising-symmetry Bose-Fermi Anderson model described by

$$\begin{aligned} \hat{H}_{\text{int}} = & \sum_{\sigma} (\epsilon_d + \frac{1}{2} U \hat{n}_{d-\sigma}) \hat{n}_{d\sigma} + V \sum_{\mathbf{k}, \sigma} (d_\sigma^\dagger c_{\mathbf{k}\sigma} + \text{H.c.}) \\ & + \frac{1}{2} g (\hat{n}_{d\uparrow} - \hat{n}_{d\downarrow}) \sum_{\mathbf{q}} (\phi_{\mathbf{q}} + \phi_{-\mathbf{q}}^\dagger). \end{aligned} \quad (4.36)$$

Here, ϵ_d is the impurity level energy, $U > 0$ is the on-site Coulomb interaction, and V is the hybridization between impurity and conduction band. In the limit where charge fluctuations at the impurity site are suppressed, the Anderson model maps onto the Kondo model under a Schrieffer-Wolff transformation.⁶² For particle-hole-symmetric impurity parameters $\epsilon_d = -\frac{1}{2}U$, the mapping takes $8\Gamma_0/\pi U \rightarrow \rho_0 J_0$ with $\Gamma_0 \equiv \pi V^2 \rho_0$ the hybridization width.

The NRG approach described above, with the standard broadening procedure Eq. (4.28) applied to Eq. (4.35), also leads also to a satisfactory description of $A(\omega)$ in the Bose-Fermi case, where the quantum phase transition is manifest as a collapse of the central Kondo resonance. All results for $A(\omega)$ were obtained for NRG discretization parameter $\Lambda = 3$, retaining $N_s = 800$ states from one iteration to the next, and taking bosonic truncation parameter $N_b = 8$. Again, the half-bandwidth D is taken to be the energy unit unless stated otherwise. We use broadening parameter $b = 0.3$, which gives the most accurate recovery of the standard $B_0 = (K_0 g_0)^2 = 0$ Fermi-liquid-theory result $A(\omega = 0) = 1/\pi\Gamma_0$ (see, e.g., Ref. 16), which is typically satisfied to within 2% within NRG.⁵² We do not vary b for $B_0 > 0$.

Fig. 24 compares the single-particle spectrum $A(\omega)$ — obtained for impurity parameters $U = -2\epsilon_d = 0.005$ [such that $A(\omega) = A(-\omega)$] and hybridization $\Gamma_0 = 5 \times 10^{-4}$ — for $B_0 = 0$ and two couplings $0 < B_0 < B_{0,c} \simeq 0.047043(1)$. The coupling to the bosonic bath has two main effects. First, the Hubbard satellite bands are displaced to higher energies from their $B_0 = 0$ positions, which in the Kondo limit ($J \ll 1$) are given by $\omega_H \simeq \pm \frac{1}{2}U$. The shift is linear in B_0 for small B_0 , as is demonstrated in Fig. 25. Second, while the central Kondo resonance remains pinned to the $B_0 = 0$ Fermi-liquid-theory result $A(\omega = 0) = 1/\pi\Gamma_0$, which remains satisfied to within 2%, its halfwidth is significantly reduced, as can be seen in the inset to Fig. 24.

At the critical coupling $B_0 = B_{0,c}$, we find that the pinning of $A(0)$ persists and the resonance has nonzero

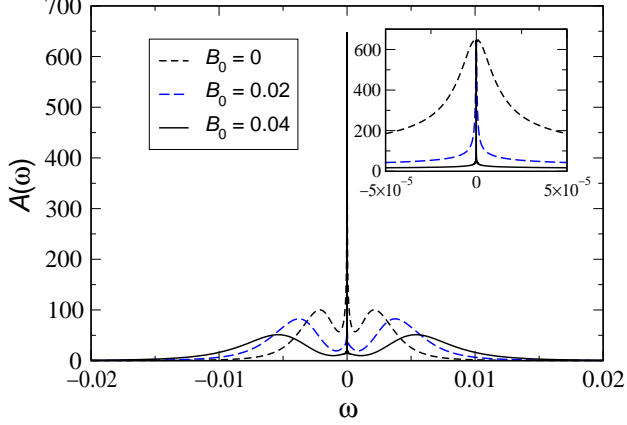


FIG. 24: (Color online). Single-particle spectrum $A(\omega)$ versus ω for $s = 0.8$, $U = -2\epsilon_d = 0.005$, $\Gamma_0 = 5 \times 10^{-4}$ and Kondo phase bosonic couplings $B_0 < B_{0,c} \simeq 0.04704$ specified in the legend. The inset shows the central resonance on an expanded scale. See text for discussion.

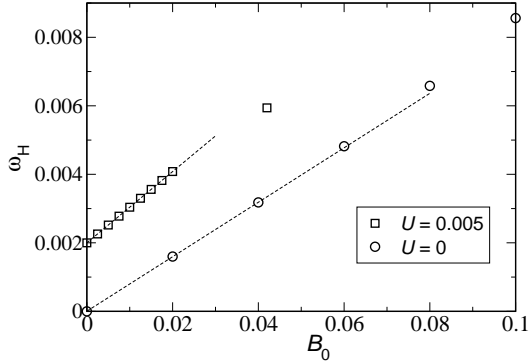


FIG. 25: Location of Hubbard band maximum ω_H as a function of bosonic bath coupling B_0 for $s = 0.8$, $\Gamma_0 = 5 \times 10^{-4}$, and the $U = -2\epsilon_d$ values shown. The dashed lines are linear fits to the data for small B_0 .

width. This is illustrated in Fig. 26, which shows three spectra: one at the QCP and one close to it in either phase. Figure 26(a) plots the spectra on the scale of the central feature and shows clearly the pinning of the critical spectrum (solid line). For $B_0 > B_{0,c}$ the Kondo resonance collapses leaving a double peak structure with characteristic scale T_* that vanishes as $B_0 \rightarrow B_{0,c}^+$. However, contrary to expectations, we find that $A(0)$ is nonzero and decreases with increasing B_0 . For fixed $B_0 > B_{0,c}$ we find that $A(0)$ does not significantly vary with N_b in the range $8 \leq N_b \leq 16$. Though the three spectra in Fig. 26 show very different behaviors at low frequencies, on the scale of the Hubbard satellite bands

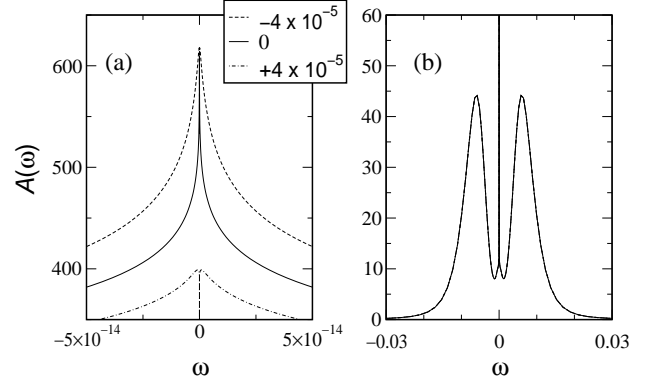


FIG. 26: Single-particle spectrum vs ω for bath exponent $s = 0.8$, impurity parameters $U = -2\epsilon_d = 0.005$, hybridization strength $\Gamma_0 = 5 \times 10^{-4}$, and discretization $\Lambda = 3$. Shown for $B_0 - B_{0,c} = 0$ (dashed line), $4 \times \pm 10^{-5}$ on (a) the scale set by the Kondo resonance; and (b) the scale of the on-site Coulomb repulsion U . The critical coupling $B_{0,c} \simeq 4.704 \times 10^{-2}$.

[see Fig. 26(b)] they are indistinguishable.

In the Kondo phase, the scale T_* , which vanishes as $B_0 \rightarrow B_{0,c}^-$, is manifest in $A(\omega)$ as the crossover scale to the Fermi liquid form $A(0) - A(\omega) \propto \omega^2$ as $\omega \rightarrow 0$.

Figure 27 shows $A(\omega)$ for $B_0 = 0$ (dotted line) and a set of B_0 values close to the critical coupling; $A(\omega)$ for $B_0 = B_{0,c}$ is shown as a thick solid line. The crossover scale T_* , at which the Fermi liquid “shoulder” is observed vanishes as $B_0 \rightarrow B_{0,c}^-$. On the localized side, the low frequency peak vanishes as $B_0 \rightarrow B_{0,c}^+$. Thus, regardless of phase, the critical spectrum is followed to progressively lower frequencies as the transition is approached. The correlation length exponent $\nu(s)$ can be calculated from the crossovers in $A(\omega)$ described, and agrees well with the values determined for the BFKM in Sec. IV.

In the quantum-critical region $|\omega| \gg T_*$, $A(\omega)$ is of form

$$A(\omega = 0) - A(\omega) \propto |\omega|^a, \quad (4.37)$$

with $A(\omega = 0) = 1/\pi\Gamma_0$ satisfied for all $0 < s < 1$ to within 2%. To extract the power a we fit the critical spectrum ($B_0 = B_{0,c}$) to the form

$$A(\omega) = [\pi\Gamma_0(1 + k|\omega|^a)]^{-1}, \quad (4.38)$$

shown as the thick dashed line in the inset to Fig. 27 for $s = 0.8$. The fit is followed well over many orders of magnitude and is ultimately cut off by the Hubbard satellite bands. Though there remains a small numerical uncertainty in the fits, largely due to the fact that the zero-frequency pinning is only satisfied to within 2%, our results suggest that $a = 1 - s$ for all $0 < s < 1$ with k a constant depending on s and T_K .

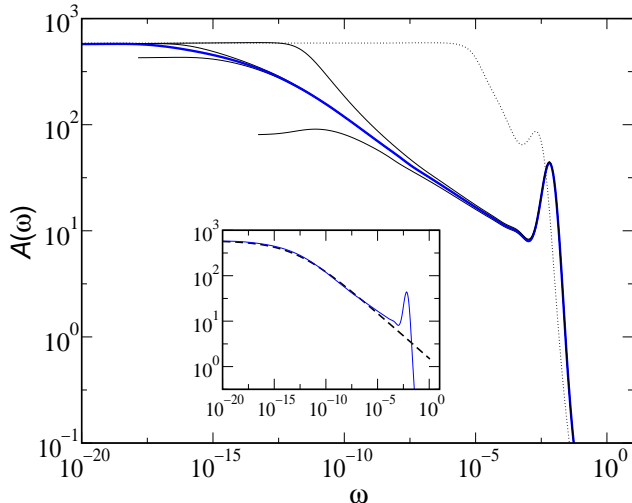


FIG. 27: (Color online) Single-particle spectrum $A(\omega)$ versus ω , shown on a logarithmic scale, for $s = 0.8$, $U = -2\epsilon_d = 0.005$, $\Gamma_0 = 5 \times 10^{-4}$, and bosonic couplings $B_0 = 0$ (dotted line), $B_{0,c}$ (thick solid line), $B_{0,c} \pm 10^{-5}$ and $B_{0,c} \pm 10^{-3}$. See text for discussion. The inset shows a fit to the QCP spectrum of form $A(\omega) = [\pi\Gamma_0(1 + k|\omega|^a)]^{-1}$ with $a = 0.2$, which is followed well over several orders of magnitude until it is cut off by the Hubbard satellite bands.

Surprisingly, the key features described above are all present in the *noninteracting* limit ($U = \epsilon_d = 0$) of the Anderson model, Eq. (4.36). Figure 28 shows the spectral function $A(\omega)$ obtained for $s = 0.8$ with $U = 0$, fixed $\Gamma_0 = 5 \times 10^{-4}$, and a sequence of increasing bosonic couplings B_0 . For $B_0 = 0$ (dotted line) the model is exactly solvable and it is well known that $A(\omega)$ has a simple Lorentzian form $A(\omega) = (\Gamma_0/\pi)/(\omega^2 + \Gamma_0^2)$, which is recovered well by the NRG broadening procedure. With increasing $B_0 < B_{0,c} \approx 0.0648$ the central peak narrows rapidly, developing symmetric shoulders that separate into distinct bands redolent of the Hubbard satellites for the regular symmetric Anderson model ($B_0 = 0$) for $U = -2\epsilon_d \gg 1$. As found for $U > 0$, the position of the satellite bands increases linearly in B_0 for small B_0 , as shown in Fig. 25. At the critical coupling the central resonance has nonzero width and remains pinned at $A(0) = 1/\pi\Gamma_0$. It is again possible to fit the critical spectrum to the form Eq. (4.38) and, as for $U = 0.005$ (Fig. 27), we find $a = 0.2$ for $s = 0.8$. This is demonstrated in the inset to Fig. 28, which shows data for $B_0 = 0.0648$ (Kondo phase) and 0.0650 (localized phase). In the frequency range shown the two data sets coincide — a reflection of the fact that $|\omega| \gg T_*$ — and are well described by the fit discussed above, which is plotted as a dashed line.

At the quantum-critical point itself we find that spec-

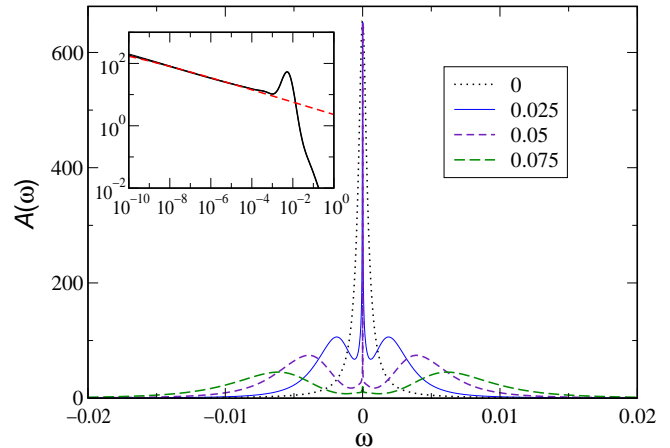


FIG. 28: (Color online) Single-particle spectrum $A(\omega)$ versus ω for non-interacting limit $U = 0$ with $\Gamma_0 = 5 \times 10^{-4}$, $s = 0.8$, and the B_0 values shown in the legend. With increasing $B_0 < B_{0,c} \approx 0.0648$ the central Lorentzian peak narrows rapidly, developing shoulders that separate from the parent peak to form distinct bands. In the quantum-critical regime ($|\omega| \gg T_*$) we find the same frequency dependence as for $U > 0$; the dashed line in the inset shows a fit of form Eq. (4.38) with $a = 0.2$ to data for $B_0 = 0.0648$ (K phase) and 0.0650 (L phase). As for $U > 0$ the localized phase spectrum contains a double peak structure about $\omega = 0$ with $A(\omega = 0) > 0$. See text for further comment.

tra scale according to

$$\pi\Gamma_0 A(\omega) = \psi_s(\omega/B_0^{1-s}), \quad (4.39)$$

as demonstrated in Fig. 29. In the vicinity of the quantum-critical point single-particle spectra scale according to

$$\pi\Gamma_0 A(\omega) = \psi_{s,p}\left(\frac{\omega}{T_*}, \frac{T_K}{T_*}\right) \quad (4.40)$$

where $p = K$ or L denotes the phase. For the QCP, where $T_* = 0$, and $B_{0,c} \propto T_K^{1-s}$, the form reduces to that of Eq. (4.39), which scaling is demonstrated explicitly in Fig. 29.

V. RESULTS: OHMIC DISSIPATION, $s = 1$

For any fixed T_K , the line of continuous quantum phase transitions in the g - s plane terminates at a Kosterlitz-Thouless-like transition at $s = 1$. As is to be expected from the well-known mapping discussed in Sec. IIB, the key physics of the BFKM with Ohmic dissipation is already present in the anisotropic Kondo model. The Ohmic BFKM corresponds to an Ohmic spin-boson

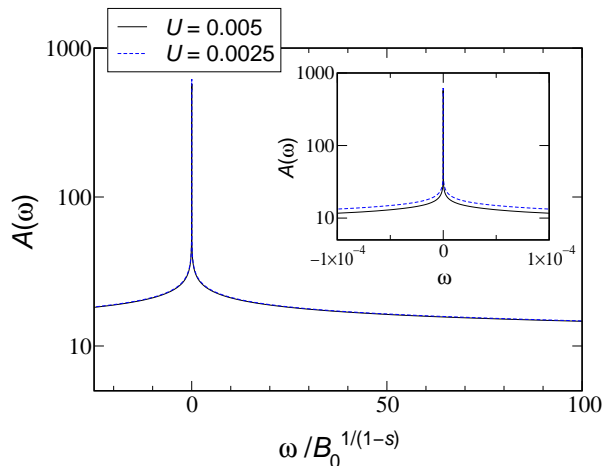


FIG. 29: (Color online) Critical single-particle spectrum $A(\omega)$ for $s = 0.8$, $U = 0.005$ and 0.0025 , $\epsilon_d = -\frac{1}{2}U$, $\Gamma_0 = 5 \times 10^{-4}$, and $B_0 = B_{0,c}$ in either case. The main figure shows scaling in terms of $B_0^{1/(1-s)} \propto T_K$, while the inset shows the two data sets on an absolute scale.

model with dissipation strength α containing contributions from the Kondo term in the Hamiltonian, Eq. (2.17) with $J_\perp = J_z = J_0$, and from B_0 , Eq. (2.14). For $B_0 = 0$ and $0 < \rho_0 J_0 \ll 1$, the resulting SBM lies in the delocalized phase with $\alpha = 1^-$; an exponentially-small renormalized tunnelling amplitude, corresponding to the Kondo scale, sets the scale for the low-energy physics. By increasing $B_0 > 0$, the system may be further driven towards a Kosterlitz-Thouless transition at $\alpha = 1$, where the renormalized tunnelling amplitude vanishes, and eventually into the localized phase $\alpha > 1$. This is, of course, the essential physical behavior of the *anisotropic* Kondo model. In other words, the principal effect of coupling to an Ohmic bosonic bath is to introduce anisotropy into the corresponding Kondo model: $\rho_0 J_\perp - \rho_0 J_z \propto B_0$.

In this section we present results of direct calculations for the Bose-Fermi Kondo and Anderson models obtained using the NRG approach described in Sec. III. We begin by discussing the Kosterlitz-Thouless nature of the NRG flow of effective couplings. We then cast results for the static local susceptibility in terms of a noisy quantum box,³ showing that perfect Coulomb-staircase behavior obtains above a critical coupling to the Ohmic bath. We conclude by discussing the single-particle spectral function for the Bose-Fermi Anderson model with Ohmic dissipation, along with its universal scaling properties.

For $s \rightarrow 1^-$ the critical fixed point merges with the weak-coupling fixed point located at $J = g = 0$, as found in Ref. 17. A schematic NRG flow diagram for $s = 1$ is given in Fig. 30. The phase boundary between Kondo-screened and localized phases is shown as a dashed line. Figure 31 shows the numerically obtained phase boundary for the Ohmic case. As expected by analogy to the AKM, $g_c^2 \propto J$ for $J \ll 1$. For $g \rightarrow g_c^-$ the NRG level flow

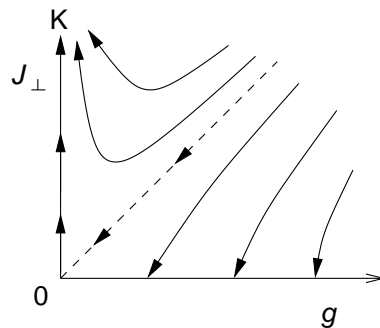


FIG. 30: Schematic of NRG flow of effective couplings for the BFKM with Ohmic dissipation. The dashed line represents the phase boundary in the J - g plane. A crossover scale T_* vanishes upon approaching the transition from the Kondo-screened phase. See text for discussion.

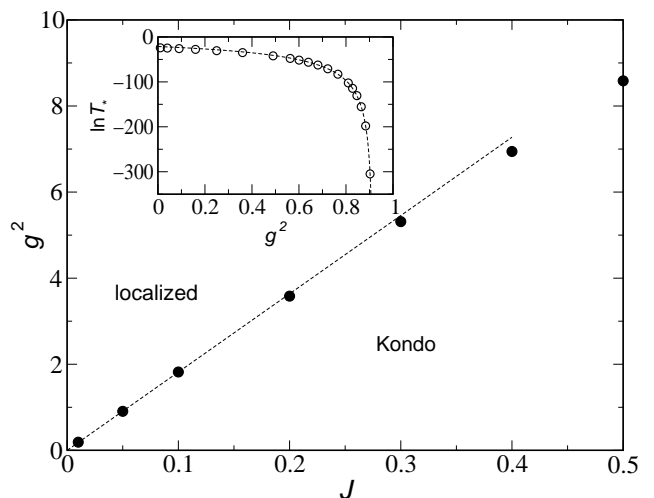


FIG. 31: Phase boundary between Kondo ($g < g_c$) and localized phases ($g > g_c$) as a function of Kondo exchange interaction J for Ohmic dissipation. For $J \ll 1$, $g_c^2 \propto J$ (dashed line). The inset shows the vanishing of the crossover scale T_* , with the latter obtained from NRG levels flows, as the phase boundary is approached from the Kondo phase for $J = 0.05$. The dashed line shows a fit to the form Eq. (5.1) with $g_c \simeq 0.958$.

is first towards the localized fixed point at $J = g = 0$. At a low-energy scale T_* (large NRG iteration number N_*), the NRG levels cross over to their stable Kondo-fixed-point values for $s = 1$. In contrast to the sub-Ohmic case $0 < s < 1$, there is no crossover scale observed when approaching the transition from the localized side, corresponding to a line of stable fixed points being reached for $g > g_c$.

The above comments are well illustrated by Fig. 32, which shows $\chi_{\text{loc}}(T; \omega = 0)$ for $s = 1$, $J = 0.5$ and a range of dissipation strengths g spanning $g_c \simeq 2.92$. The observed behavior should be compared to that of Fig. 12 for $s = 0.5$, which is typical of the sub-Ohmic case

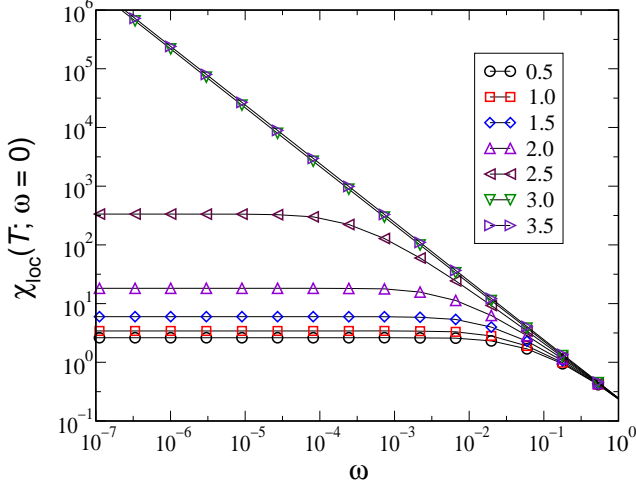


FIG. 32: (Color online) $\chi_{\text{loc}}(T; \omega = 0)$ versus T for the Ohmic case $s = 1$, $J = 0.5$ and bosonic couplings shown; $g_c \simeq 2.92$. On the Kondo side, a clear crossover scale exists, equivalent to the renormalized Kondo scale $\chi_{\text{loc}}^{-1}(0, 0)$, and vanishes continuously as $g \rightarrow g_c^-$. No such scale is present for the localized phase. Data obtained for $\Lambda = 9$, $N_b = 12$, and $N_s = 800$. See text for further comment.

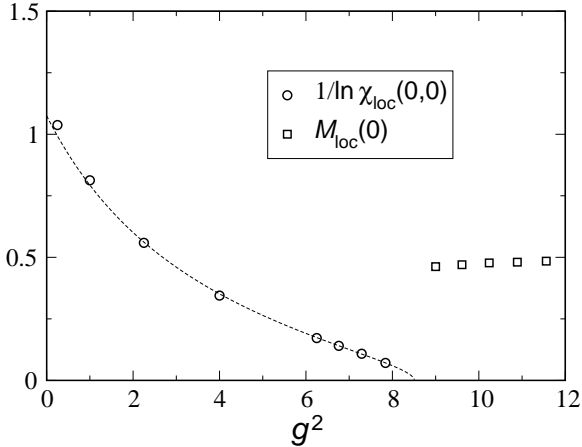


FIG. 33: Behavior of the renormalized Kondo scale $\chi_{\text{loc}}^{-1}(T = 0, \omega = 0)$ ($\propto T_*$ for $s = 1$) and the order parameter $M_{\text{loc}}(T = 0)$ for the Ohmic case $s = 1$ and $J = 0.5$. The dashed line is a fit of form Eq. (5.1). In the Ohmic case the order parameter undergoes a clear jump at the transition point $g = g_c \simeq 2.92$. See text for further discussion.

$s < 1$. For Ohmic dissipation and $g < g_c$, the impurity spin is quenched below a crossover scale T_* that vanishes continuously as $g \rightarrow g_c^-$. The renormalized Kondo scale $\chi_{\text{loc}}(0, 0)^{-1}$ ($\propto T_*$ for $s = 1$) likewise vanishes and we

find

$$\ln T_* = a_0 - \frac{a_1}{\sqrt{g_c^2 - g^2}}. \quad (5.1)$$

Such a form follows from a poor-man's scaling analysis for the anisotropic Kondo model,⁶³ which can be shown to yield

$$T_K = D \exp \left(1 + \frac{1}{|\rho_0 J_z|} - \frac{\pi}{\delta} \right), \quad (5.2)$$

which holds for $0 \ll \delta \ll -\rho_0 J_z$ close to the transition with $\delta^2 = (\rho_0 J_\perp)^2 - (\rho_0 J_z)^2$, and recognizing that $g_c^2 - g^2 \propto (\rho_0 J_\perp - \rho_0 |J_z|) \simeq \delta^2 / 2J$. A fit to the behavior Eq. (5.1) is shown in Fig. 33, yielding a value for $g_c \simeq 2.92$ in good agreement with that obtained via NRG level flows. The corresponding fit for $J = 0.05$ is shown in the inset to Fig. 31. The constants a_0 and a_1 vary as $1/\sqrt{J}$ for $J \ll 1$, as expected from Eq. (5.2).

For $T \gg T_*$, we find $\chi_{\text{loc}}(T; \omega = 0) \propto T^{-1}$ with logarithmic corrections. For $g > g_c$, $\chi_{\text{loc}}(T; \omega = 0) \propto 1/T$ shows Curie-like behavior characteristic of a freely fluctuating spin. However, as $g \rightarrow g_c^+$, the order parameter $M_{\text{loc}}(0)$ does not vanish continuously, but rather jumps to zero at $g = g_c$ with the size of the jump being roughly 90% of the full saturation value.

The noisy quantum box.—The case of Ohmic dissipation in the BFKM has recently been studied in the context of gate-voltage fluctuations in a quantum box. A quantum box consists of a small metallic grain (or dot) with a dense spectrum coupled to reservoir leads. Gate electrodes control the electrostatic energy of the dot,

$$E_Q = \frac{(Q - eN)^2}{2C}, \quad (5.3)$$

where N is proportional to the gate voltage, Q is the charge on the dot and C the capacitance. Degeneracy points at half-integer values of N (where $E_Q = E_{Q-e}$) lead to a unit jump in the number of electrons on the grain at that point, and thus to the familiar Coulomb-blockade “staircase” behavior for $\langle Q \rangle$ versus N . However, the sharp charging steps are rounded due to quantum fluctuations, as shown theoretically by Matveev⁶⁴ by mapping the problem to a two-channel Kondo model. Le Hur has recently shown³ that the suppression of quantum charge fluctuations due to the dissipative effects of a fluctuating gate voltage can restore perfect Coulomb-staircase behavior. This has been discussed in the context of a Bose-Fermi Kondo model, where the “spin” states of the impurity correspond to the two charge states (orbital pseudospin) of the grain close to a degeneracy point. Considering charging states $Q = 0$ and $Q = 1$ leads to the identification $\langle S_z \rangle = \langle Q \rangle - \frac{1}{2}$. The electrons themselves are taken to be spinless, thus assuming the presence of a strong in-plane magnetic field. The gate voltage, which controls deviations away from the degeneracy point, i.e., differences in the energies of the spin states, plays the role of the local magnetic field h in the impurity problem.

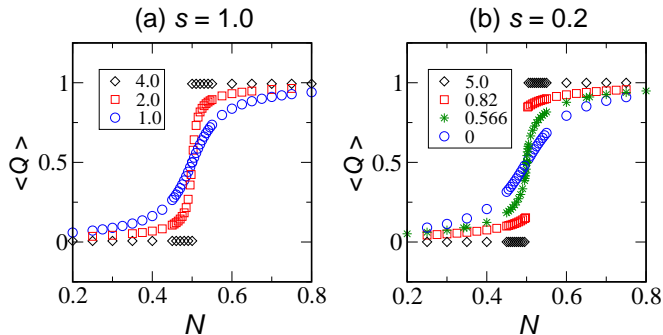


FIG. 34: (Color online) Average charge on dot $\langle Q \rangle$ versus gate voltage N , for the noisy quantum dot system with (a) Ohmic and (b) sub-Ohmic dissipation. The legends specify the dissipation strength g in the BFKM. For weak dissipation the curves $\langle Q \rangle$ versus N are linear through the degeneracy point $N = \frac{1}{2}$ due to Kondo screening of local moments. In the Ohmic case (a), the curves undergo a large jump at $N = \frac{1}{2}$ for $g \geq g_c \simeq 2.92$. For $g = g_c \simeq 0.566$ in the sub-Ohmic case (b), $\langle Q \rangle - \frac{1}{2}$ vanishes in a power-law fashion at $N = \frac{1}{2}$, while for increasing $g > g_c$ it exhibits a jump of a magnitude that increases continuously from zero.

The Kondo term represents tunneling from lead to grain and vice versa, while the bosonic bath, which is Ohmic, represents the voltage fluctuations. It then follows that

$$\frac{\partial \langle Q \rangle}{\partial N} \propto \frac{\partial \langle S_z \rangle}{\partial h}. \quad (5.4)$$

The static susceptibility $\chi_{\text{loc}}(0,0)$ thus measures the slope of $\langle Q \rangle$ versus N at the degeneracy point $N = \frac{1}{2}$. Our results indeed show a perfect restoration of the Coulomb staircase for large enough coupling to the bosonic environment. Figure 34(a) shows $\langle Q \rangle$ versus N plots for the Ohmic case where perfect Coulomb staircase behavior is restored for $g \geq g_c$. That there is a jump in $\langle Q \rangle$ for $g = g_c$ itself stems from the Kosterlitz-Thouless nature of the transition discussed above. For sub-Ohmic baths, by contrast, a continuous critical curve obtains at $g = g_c$, with a slope that is infinite at $N = \frac{1}{2}$. For increasing $g > g_c$, the size of the jump in $\langle Q \rangle$ at $N = \frac{1}{2}$ increases from zero, consistent with the behavior of $M(0)$ in Fig. 33. Our NRG results, which solve the Ohmic BFKM directly, are consistent with the picture described by perturbative RG³ and by a bosonic NRG treatment following the mapping of the BFKM to a spin-boson model.⁴

We now turn to a discussion of spectral functions for the Bose-Fermi Anderson model with Ohmic dissipation. Figure 35 shows spectra for fixed $U = -2\epsilon_d = 0.005$ and $\Gamma_0 = 5 \times 10^{-4}$, for which the corresponding $J \simeq 0.25$, and a sequence of increasing dissipation strengths B_0 . There are several key differences compared to the sub-Ohmic case. First, and most obviously, the spectrum at the critical coupling $B_0 = B_{0,c} \simeq 0.33$ is not pinned to the Kondo phase value $A(\omega = 0) = (\pi\Gamma_0)^{-1}$, but is much

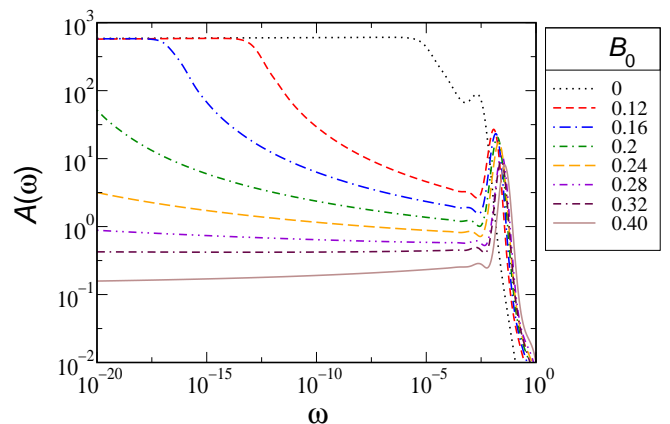


FIG. 35: (Color online) Single particle spectrum $A(\omega)$ versus ω for the Ohmic case $s = 1$ and $U = -2\epsilon_d = 0.005$, $\Gamma_0 = 5 \times 10^{-4}$, and the B_0 values shown. See text for comments.

reduced. Furthermore, there is essentially no frequency dependence to the critical spectral function below scales on the order of the Hubbard satellite bands. For the parameters considered in Fig. 35, $A(\omega = 0) \simeq 0.5$ at the critical coupling. This form is followed by the $B_0 = 0.32$ data down to $T_* \simeq 10^{-120}$ which sets the scale for crossover to Kondo-phase behavior.

Second, the vanishing of the crossover scale T_* , describing, e.g., the vanishing of the Kondo resonance half-width, is well fit by

$$\ln T_* \propto a_0 - \frac{a_1}{\sqrt{B_{0,c} - B_0}} \quad (5.5)$$

as expected from the result Eq. (5.1) for the Ohmic Bose-Fermi *Kondo* model.

Third, the Kondo-phase spectra obey a simple scaling form

$$\pi\Gamma_0 A(\omega) = \phi_{s=1,K} \left(\frac{\omega}{T_*} \right), \quad (5.6)$$

as shown in Fig. 36(b). The spectra there plotted, which have vastly different crossover scales (see, e.g., Fig. 35), collapse to the single universal curve Eq. (5.6), which form is followed up to the nonuniversal energy scale set by the Hubbard satellite bands, ω_H/T_* . For the data shown, excellent data-collapse is seen up to $\omega/T_* \simeq 10^7$.

We note that calculations of the T -matrix in Ref. 5, discussed in the context of the quantum box, are in qualitative agreement with the above.

VI. SUMMARY

We have described an extension of Wilson's numerical renormalization group method appropriate for Bose-Fermi quantum impurity models. We have focused in particular on the Ising anisotropic Bose-Fermi Kondo

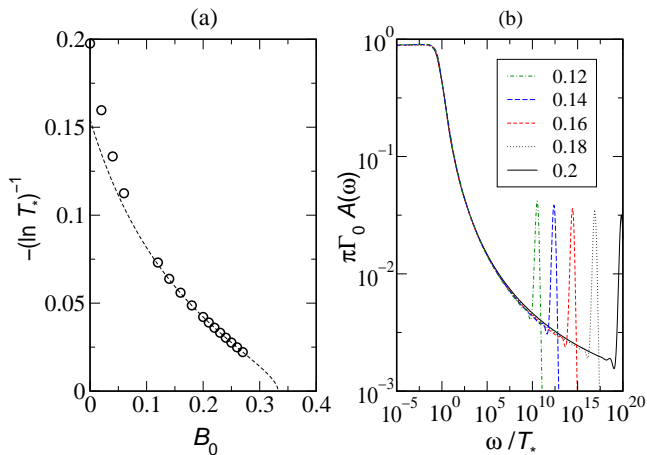


FIG. 36: (Color online) (a) Vanishing of crossover scale T_* for $B_0 \rightarrow B_{0,c}^-$, according to Eq. (5.5) (dashed line). (b) Scaling of the single-particle spectrum $\pi\Gamma_0 A(\omega)$ for the dissipation strengths B_0 shown in the inset. Though the values of T_* in this data set vary across ten orders of magnitude, a single universal scaling curve [Eq. (5.6)] is followed up to the nonuniversal scale set by the Hubbard satellite bands.

model. The approach gives an excellent description of the critical properties of this model, which is of relevance to certain dissipative mesoscopic qubit devices and to a treatment of the anisotropic Kondo lattice model within an extension of dynamical mean-field theory.²³ For sub-Ohmic bosonic bath exponents $0 < s < 1$ we find a continuous quantum phase transition between Kondo-

screened and localized phases. The transition is governed by an interacting quantum-critical point, leading to hyperscaling of critical exponents and ω/T -scaling in the dynamics. We have shown directly that the Kondo resonance in the spectral function is destroyed at the critical point. The case of Ohmic dissipation, which leads to a Kosterlitz-Thouless like transition, was also discussed.

While we have specifically studied the case of Ising symmetry bosonic couplings, the approach is not per se limited to that case. It is straightforward, albeit computationally more demanding, to add additional bosonic bath(s) as appropriate for the xy -anisotropic or isotropic Bose-Fermi Kondo models. These cases will be discussed elsewhere. Furthermore, our approach could be integrated with the recently developed time-dependent NRG method^{65,66} to enable the study of nonequilibrium dynamics for a wider range of quantum impurity systems. Other models that might be tackled using the present approach include an Anderson-Holstein-type model (where the impurity charge density couples to a bosonic bath) relevant to the study of electron-phonon interactions in strongly correlated electron systems, and novel Bose-Fermi impurity problems that may arise in the treatment of ultracold mixtures of bosonic and fermionic atoms trapped in optical lattices. These applications are left for future study.

We thank Q. Si and R. Bulla for stimulating discussions regarding the present work. Much of the computational work was performed using the University of Florida High Performance Computing Cluster; we thank C. Taylor in particular for technical support. This work was supported in part by NSF Grant DMR-0312939.

* Electronic address: glossop@phys.ufl.edu

¹ A. J. Leggett *et al.*, *Rev. Mod. Phys.* **59**, 1 (1987).

² U. Weiss, *Quantum dissipative systems* (World Scientific, Singapore, 1999).

³ K. Le Hur, *Phys. Rev. Lett.* **92**, 196804 (2004).

⁴ M. R. Li, K. Le Hur, and W. Hofstetter, *Phys. Rev. Lett.* **95**, 086406 (2005).

⁵ L. Borda, G. Zaránd, and P. Simon, *Phys. Rev. B* **72**, 155311 (2005).

⁶ M. Thorwart and P. Hanggi, *Phys. Rev. A* **65**, 012309 (2002).

⁷ T. A. Costi and R. H. McKenzie, *Phys. Rev. A* **68**, 034301 (2003).

⁸ M. J. Storcz and F. K. Wilhelm, *Phys. Rev. A* **67**, 042319 (2003).

⁹ D. V. Khveshchenko, *Phys. Rev. B* **68**, 193307 (2003).

¹⁰ A. Garg, J. N. Onuchic, and V. Ambegaoker, *J. Chem. Phys.* **83**, 4491 (1985).

¹¹ S. Tornow, N. H. Tong, and R. Bulla, *Europhys. Lett.* **73**, 913 (2006).

¹² R. Bulla, *Phil. Mag.* **86**, 1877 (2006).

¹³ H. J. Lee and R. Bulla, *arXiv:cond-mat/0606325* (2006).

¹⁴ K. G. Wilson, *Rev. Mod. Phys.* **47**, 773 (1975).

¹⁵ J. L. Smith and Q. Si, *Europhys. Lett.* **45**, 228 (1999).

¹⁶ A. C. Hewson, *The Kondo Problem to Heavy Fermions* (Cambridge University Press, Cambridge, U.K., 1993).

¹⁷ L. Zhu and Q. Si, *Phys. Rev. B* **66**, 024426 (2002).

¹⁸ G. Zaránd and E. Demler, *Phys. Rev. B* **66**, 024427 (2002).

¹⁹ M. Vojta, *Phil. Mag.* **86**, 1807 (2006).

²⁰ S. Kirchner, L. Zhu, Q. Si, and D. Natelson, *Proc. Natl. Acad. Sci.* **102**, 18824 (2005).

²¹ Q. Si, S. Rabello, K. Ingersent, and J. L. Smith, *Nature (London)* **413**, 804 (2001).

²² Q. Si, S. Rabello, K. Ingersent, and J. L. Smith, *Phys. Rev. B* **68**, 115103 (2003).

²³ M. T. Glossop and K. Ingersent, *arXiv:cond-mat/0607566* (2006).

²⁴ J. X. Zhu, S. Kirchner, R. Bulla, and Q. Si, *arXiv:cond-mat/0607567* (2006).

²⁵ J. A. Hertz, *Phys. Rev. B* **14**, 1165 (1976).

²⁶ D. R. Grempel and Q. Si, *Phys. Rev. Lett.* **91**, 026401 (2003).

²⁷ J.-X. Zhu, D. R. Grempel, and Q. Si, *Phys. Rev. Lett.* **91**, 156404 (2003).

²⁸ P. Sun and G. Kotliar, *Phys. Rev. Lett.* **91**, 037209 (2003).

²⁹ D. Tanasković, V. Dobrosavljević, and E. Miranda, *Phys.*

- Rev. Lett. **95**, 167204 (2005).
- ³⁰ K. Haule, A. Rosch, J. Kroha and P. Wolfle, Phys. Rev. B **68**, 155119 (2003).
- ³¹ A. C. Hewson and D. Meyer, J. Phys. Condens. Matter **14**, 427 (2002).
- ³² W. Koller, D. Meyer, and A. C. Hewson, Phys. Rev. B **70**, 155103 (2004).
- ³³ W. Koller, D. Meyer, Y. Ono, and A. C. Hewson, Europhys. Lett. **66**, 559 (2004).
- ³⁴ C. Gonzalez-Buxton and K. Ingersent, Phys. Rev. B **57**, 14254 (1998).
- ³⁵ R. Bulla, M. T. Glossop, D. E. Logan, and T. Pruschke, J. Phys. Condens. Matter **12**, 4899 (2000).
- ³⁶ L. Borda *et al.*, Phys. Rev. Lett. **90**, 026602 (2003).
- ³⁷ M. R. Galpin, D. E. Logan, and H. R. Krishnamurthy, Phys. Rev. Lett. **94**, 186406 (2005).
- ³⁸ V. Meden and F. Marquardt, Phys. Rev. Lett. **96**, 146801 (2006).
- ³⁹ L. G. G. V. Dias da Silva, N. P. Sandler, K. Ingersent, and S. E. Ulloa, Phys. Rev. Lett. **97**, 096603 (2006).
- ⁴⁰ K. Ingersent, A. W. W. Ludwig, and I. Affleck, Phys. Rev. Lett. **95**, 257204 (2005).
- ⁴¹ R. Bulla, T. A. Costi, and D. Vollhardt, Phys. Rev. B **64**, 045103 (2001).
- ⁴² T. Pruschke, R. Bulla, and M. Jarrell, Phys. Rev. B **61**, 12799 (2000).
- ⁴³ A. C. Hewson, S. C. Bradley, R. Bulla, and Y. Ono, Int. J. Mod. Phys. B **15**, 2549 (2001).
- ⁴⁴ R. Bulla, N. H. Tong, and M. Vojta, Phys. Rev. Lett. **91**, 170601 (2003).
- ⁴⁵ R. Bulla, H. J. Lee, N. H. Tong, and M. Vojta, Phys. Rev. B **71**, 045122 (2005).
- ⁴⁶ M. T. Glossop and K. Ingersent, Phys. Rev. Lett. **95**, 067202 (2005).
- ⁴⁷ T. A. Costi and G. Zaránd, Phys. Rev. B **59**, 12398 (1999).
- ⁴⁸ M. Vojta, N. H. Tong, and R. Bulla, Phys. Rev. Lett. **94**, 070604 (2005).
- ⁴⁹ H. R. Krishna-murthy, J. W. Wilkins, and K. G. Wilson, Phys. Rev. B **21**, 1003 (1980).
- ⁵⁰ C. Lanczos, J. Res. Natl. Bur. Stand. **45**, 255 (1950).
- ⁵¹ R. Bulla, private communication.
- ⁵² T. A. Costi, A. C. Hewson, and V. Zlatić, J. Phys. Condens. Matter **6**, 2519 (1994).
- ⁵³ The results of the Ref. 46 correspond under the current formulation to $\tilde{\omega}_0 = \frac{1}{3}$.
- ⁵⁴ L. N. Oliveira and J. W. Wilkins, Phys. Rev. B **24**, 4863 (1981).
- ⁵⁵ S. Sachdev, *Quantum Phase Transitions* (Cambridge University Press, Cambridge, U.K., 1999).
- ⁵⁶ O. Sakai, Y. Shimizu, and T. Kasuya, J. Phys. Soc. Jpn **58**, 3666 (1989).
- ⁵⁷ K. Ingersent and Q. Si, Phys. Rev. Lett. **89**, 076403 (2002).
- ⁵⁸ M. T. Glossop, G. E. Jones, and D. E. Logan, J. Phys. Chem. B **109**, 6564 (2005).
- ⁵⁹ L. Fritz, S. Florens, and M. Vojta, arXiv:cond-mat/0604603 (2006).
- ⁶⁰ M. E. Fisher, S. Ma, and B. G. Nickel, Phys. Rev. Lett. **29**, 917 (1972).
- ⁶¹ J. M. Kosterlitz, Phys. Rev. Lett. **37**, 1577 (1976).
- ⁶² J. R. Schrieffer and P. A. Wolff, Phys. Rev. **149**, 491 (1966).
- ⁶³ P. W. Anderson, G. Yuval, and D. R. Hamann, Phys. Rev. B **1**, 4464 (1970).
- ⁶⁴ K. A. Matveev, Zh. Eksp. Teor. Fiz. **98**, 1598 (1990).
- ⁶⁵ F. B. Anders and A. Schiller, Phys. Rev. Lett. **95**, 196801 (2005).
- ⁶⁶ F. B. Anders and A. Schiller, arXiv:cond-mat/0604517 (2006).